CHAPTER 2 LITERATURE REVIEWS AND THEORY

2.1 Literature reviews of laser ablation

The laser ablation has main steps to form nanostructures from target immersed in liquid. First, heat up the target surface to high temperature, and thus plasma containing vapor atoms of target is occurred. Then plasma expands adiabatically and finally nanoparticles will be generated when condensation occurs. During this step first, nucleation takes place; then fine nuclei either collide and stick together. For nanoparticles simulated and synthesized by laser ablation has relevant research follows.

Lunney *et al.* [22] have created a simple model for physical behavior in laser heating and vaporization of metal substrate. Laser absorption and heating of vaporised material, ionization dynamics, and re-radiation to target are combined. The simulation model was used to determine plasma absorption, the average ion energy and ablation depth per pulse for iron target. The results were compared with the experimental results.

Sonntag *et al.* [23] simulated a femtosecond laser ablation of aluminum with two equations to solve simultaneously for electronic system which for laser energy absorption and heat conduction by finite element method , the other for dynamic lattice where the laser ablation take place by common molecular dynamic. The results of hybrid simulation were investigated.

Nedialkov *et al.* [24] did theorical and experimental in laser ablation of iron. The experiments used Ti:sapphire laser with pulse duration of 0.1 picosecond. Ablation rate and surface structures were determined. Different powers are applied to the target. The molecular dynamics simulation was technique to describe the process

De-zhi [25] created the unified model that introduced the electron-phonon coupling time for substitute thermal model (long pulses) and standard two temperature model (short pulses).It used thermal and optical of gold parameters for this simulation. The temperature of surface at difference depth, energies of laser and pulse width were investigated.

Leitz *et al.* [26] studied about effect of number of pulse to depth and drill hole of stanless steel samples with the four ranges of pulse width (micro, nano, pico and femtosecond) of pulsed laser ablation. The efficiencies of pulse width of laser energies were compared. The short pulsed in micro and nanosecond have high ablation rates but thermal damage of the workpiece cannot be avoided completely. Ultrafast pico and femtosecond systems have a higher precision but lower ablation efficiency.

Stratakis *et al.* [27] reported the formation of nanostructure on bulk aluminum (Al) in air and liquid media with a pulse laser in femtoseconds. The average size of achieved product on Al surface was about 200 nm after investigating by transmission electron microscopy (TEM), FE-SEM, atomic force microscopy (AFM), and UV visible absorption spectrophotometer

Kim *et al.* [28] synthesized silver nanoparticles in distilled water by Nd:YAG laser 355 nm with energy 160mJ/pulse, . The size and morphology were investigated by TEM and the structures of nanoparticles were confirmed by XRD. It is shown that the process is effective for preparing nanoparticle suspensions having relatively uniform size distributions. While the laser fluence strongly influence the size of the produced nanoparticle in air, the sedimentation time is shown to be the most critical factor to determine the mean size of the suspended particles.

Gondal *et al.* [29] reported the preparation of nikel oxide (NiO) nanoparticles by irradiated third harmonic 355nm Nd:YAG laser operating at 10 Hz, 30 minutes to nikel target immersed in 3% H_2O_2 liquid solution. XRD confirms the formation of pure NiO with lattice constant 0.42033 nm and nanosize of about 8 nm which is verified by FESEM. The EDS quantitative analysis clearly reveals the presence of only nickel and oxygen with no impurities. FTIR spectra confirm the bond between nickel and oxygen at around 450 cm^{-1}.

Nikolov *et al.* [30] synthesized TiO_x by pulsed-laser ablation of titanium disk targets in water. Nd:YAG (wavelength 532 nm, pulse duration 15 ns and repetition rate 2 Hz) with different laser energies in the interval from 40 to 120 mJ/pulse, respectively 4.1–12.4 J/cm^2, and the processing time was 30 min. NPs produced at lower fluences (4.1 and 8.2 J/cm^2) have spherical form and are amorphous, whereas some of those produced at higher fluence (12.4 J/cm^2) crystallize. Thus, a transition of the NPs structure from amorphous to crystalline as the laser energy increased is revealed. Aggregation of the created particles during aging was found. Transition of the NPs' structure from amorphous to crystalline with increasing the laser energy was revealed. A difference was observed in the transmittance of the suspensions obtained depending on the laser intensity.

Pan *et al.* [31] synthesized γ-Al_2O_3 core and amorphous Al_2O_3 shell by pulsed laser ablation (Nd:YAG laser, wavelength 1064 nm, energy 1100 mJ/pulse, repetition rate 10 Hz, pulse duration 240 μs, power density of 1.5×10^8 W/cm^2, focusing beam 0.03 mm^2, ablation time 30 min) on Al target in different oxygen gas flow rates (30 and 50 l/min). The condensation, nucleation and growth of Al_2O_3 were studied in this paper and The results of experiments were characterized by Transmission Electron Microscopy (TEM) in high resolution transmission electron microscope (HRTEM), selected area electron diffraction (SAED) and energy dispersive spectroscopy (EDS).

Sima *et al.* [32] synthesized the oxide nanoparticles of Sn, In, Zn, Ni, Al, Ti and Fe target by pulse laser ablation under flow of oxygen(0.5 l/min) at pressure of 200 mbar. Nd:YAG laser was used at a wavelength of 355 nm(3rd harmonic) with laser pulse of 60 mJ energy, repetition rate 10 Hz, pulse duration 5 ns and laser fluence 5 J/cm^2. The oxide of nanoparticles were investigated by TEM in mode SAED, HRTEM

Pan *et al.* [33] synthesized α,γ-Al_2O_3 nanoparticles by pulse laser ablation under flow of oxygen(15-50 l/min) at pressure of 200 mbar. Nd:YAG laser was used at a wavelength of 1064 nm with laser pulse energy of 350, 430, 500, 830 and 1100 mJ, repetition rate 10 Hz, pulse duration 250 μs, power density 4.9×10^7, 6.0×10^7, 7.0×10^7 1.2×10^8, 1.5×10^8 W/cm^2 and focused area 0.03 mm^2.The nanoparticles were investigated by TEM in mode SAED, HRTEM, XRD and EDS

The aluminum and aluminum oxide nanoparticles synthesized by laser ablation in liquid were showed in table 2.1.

Table 2.1 The aluminum and aluminum oxide were synthesized by laser ablation in liquid.

Target	Liquid	Product	Laser source	Ref
α-Al_2O_3 sheet purity 99.7 %	Deionized water (DI water)	γ-Al_2O_3 Spherical nanoparticles size 5-120 nm average size 17- 29 nm	CW-fibre laser, 1070 nm 800 W, 1000 W, ablation time 1.5, 3 sec, spot size 70 μm	[34]
Pressed α-Al_2O_3 sheet purity 97.5 % grain size 5 μm	Distilled water	α-Al_2O_3 Spherical nanoparticles size 5 - 20 nm	Nd:YLF laser, 1047 nm, FWHM 20-60 ns, maximum pulse energy 4.6 mJ, repetition rate 4-15 Hz, scan speed 50-1400 mm/s, ablation time 5, 10, 15, 20, 25 and 30 min	[35]
Al plate thickness 1 mm, purity 99.9%	DI water	γ,θ-Al_2O_3 Spherical nanoparticles size 10-2000 nm	Nd:YAG laser, 1064 nm, 850 mJ/pulse, time duration 16 ns, repetition rate = 10 Hz, focus area = 0.03 mm^2,average peak power = 2.8 × 10^4 W/cm^2, Peak power density = 1.8 × 10^{11} W/cm^{2}2nd harmonic 532 nm, 400 mJ/ pulse, Average peak power = 1.3 × 10^4 W/cm^2, Peak power density = 8.3 × 10^3 W/cm^2, 3000 pulse, ablation time 5 min.	[36]
Al sheet purity 99.4%	Ethanol 99.6%	Al Spherical nanoparticles size 10-120 nm, average size = 48 nm	Nd:YAG 1st, 2st harmonic 1064 nm, 533 nm, 280-320 mJ/pulse, repetition rate 10 Hz, FWHM = 6 ns, beam diameter = 3mm, focal length = 100 mm, Ablation time 5, 10 and 15 min, Position change every 3 - 4 min	[37]

Table 2.1 The aluminum and aluminum oxide were synthesized by laser ablation in liquid(cont.)

Target	Liquid	Product	Laser source	Ref
Bulk Al	Ethanol + H_2(gas)	Al_2O_3 Spherical nanoparticles size 10-140 nm	Nd:YAG, 1.06 μm, repetition rate 10 Hz, pulse width 30 ps, exposure time 1 hour, Fluence = 4 J/cm^2	[38]
Bulk Al purity 99.999 %	Distilled water + Ethanol	Amorphous Al_2O_3 spherical nanoparticle 10-1000 nm with hollow microparticle	Pulsed KrF excimer, 248 nm, repetition rate10 Hz, pulse duration 30 ns, laser fluence 2.3 J/cm^2, spot size 1.2 mm^2	[39]
Bulk Al diameter 1 inch	Water + Ethanol ratio 3:1	γ,θ-Al_2O_3 Spherical nanoparticles size 0.1-1 μm with hollow particle	Pulsed KrF excimer, 248 nm, repetition rate 10 Hz, pulse duration 30 ns, laser fluence 5.9 J/cm^2, ablation time 30 min	[40]
Bulk Al	Acetone, Ethanol, Ethylene Glycol	Al spherical nanoparticle 15-110 nm, average size = 30-50 nm	Nd:YAG, 1064 nm, FWHM 6 ns, repetition rate 10 Hz, energy 280 – 420 mJ/pule, ablation time 5, 10 and 15 min, focal length 100 mm, beam size 3 mm^2	[41]
Bulk Al purity 99.999 %	Oleic acid (OA) + Tetrahydrofuran (THF) 0.001 M	Al Spherical nanoparticles size 10-200nm	Nd:YAG, 1064 nm, energy 0.88 J/pulse, repetition rate 20 Hz, ablation time 5 min, focal length 300 mm, spot size 1 mm	[42]
Al plate purity 99.9%	DI water + 0.05-1 M NaOH	$NaAlO_2\cdot 5/4H_2O$, $\beta NaAlO_2$, γ-Al_2O_3	Nd:YAG, 1064 nm, time duration 16 ns, repetition rate 10 Hz, focus area 0.03 mm^2,pulse energy 820 mJ/pulse, average peak power 2.8 × 10^4 W/cm^2,peak power density = 1.8 × 10^{11} W/cm^2, 3000 pulse, ablation time 5 min, 5000 pulses	[43]

Table 2.1 The aluminum and aluminum oxide were synthesized by laser ablation in liquid(cont.)

Target	Liquid	Product	Laser source	Ref
Bulk Al, Bulk Ti Purity 99%	H2O + Ethanol + H_2(gas)	Al spherical nanoparticle size < 50 nm Al spherical nanoparticle size 10-150 nm	1) Copper vapor laser, 510.6 nm, pulse duration 15 ns, fluence 10 J/cm^2, repetition rate15 kHz, 2) Ti:sapphire laser, 800 nm, pulse duration 180 fs, fluence 2 J/cm^2, repetition rate 1 kHz 3) Nd:YAG, 1064 nm, pulse duration 70 ns, repetition rate 2 kHz	[44]
Bulk Al Purity 99%	Air , water, Ethanol	Al Spherical nanoparticles size 10-200nm	Ti:sapphire laser, 800 nm, pulse duration 180 fs, fluence 2 J/cm^2, repetition rate 1 kHz	[45]

2.2 Alumina [46]

2.2.1 Structure of alumina phases

The properties of the aluminas are determined mainly by the crystal structure. In general, the phases of most significance in alumina are those produced by pseudomorphic dehydration.

Powder X-ray methods for determining crystal structure are not as suitable as single crystal methods. In many cases, however, the lack of single crystals of the alumina phases as coarse as one or two tenths of a millimeter has restricted the development of exact information. Lack of this information on the atom parameters has thrown some doubt on the named structure or crystal system for some phases. The crystalline structures of the alumina phases are shown in Table 2.2

The crystalline modifications of alumina are without exception, classed as ionic. For the arrangement of ions in lattice, the coordination number of the cations is of paramount importance. The relatively small Al^{3+} cation is usually 6-coordinated with respect to O^{2-} or $(OH)^-$ anions and is located in the interstices of octahedral anion groups. It may appear at the center of tetrahedral anion groups. It may appear at the center of tetrahedral group of 4-coordination, as in glass and in mullite. The Pauling principle of coordination is generally satisfied within each octahedron even with different kinds of octahedral coupling but in any case, neutralization is obtained at least for each separate unit cell.

In the crystal lattices of the alumina phases both cubic and hexagonal close packing may take place. In cubic close-packing of the densest arrangement, the ions of one plane occupy the hollows formed by three ions of the next plane. Every forth plane of superposition in the crystal lattice repeats to yield the face-center cubic cell

Table 2.2 Crystal structure of aluminas [46]

Phase	Crystal system	Space group	Mole-cules	Unit cell parameters (Angstroms)			Angle
				a	b	c	
Hydrated aluminas							
Gibbsite α-Al_2O_3·$3H_2O$	Monoclinic	$C_{2}^{5}h$	4	8.641	5.070	9.720	85°26´
Bayerite β-Al_2O_3·$3H_2O$	Monoclinic	$C_{2}^{5}h$	2	4.716	8.679	5.060	90°07´
Nordstrandite Al_2O_3·$3H_2O$	Monoclinic		8	8.63	5.01	19.12	92°00´
Boehmite α-Al_2O_3·$3H_2O$	Orthorhombic	$D_{2}^{17}h$	2	2.868	12.227	3.700	-
Dispore β-Al_2O_3·$3H_2O$	Orthorhombic	$D_{2}^{16}h$	2	4.396	9.426	2.844	-
Transition Aluminas							
Chi	Cubic		10	7.95	-	-	-
Eta	Cubic (spinel)	$O_{2}^{7}h$	10	7.90	-	-	-
Gamma	Tetragonal	-	-	7.95	7.95	7.79	-
Delta	Tetragonal	-	32	7.957	7.967	23.47	-
Iota	Orthorhombic	-	4	7.73	7.78	2.92	-
Theta	Monoclinic	$C_{2}^{3}h$	4	5.63	2.95	11.86	-
Kappa	Orthorhombic	-	32	8.49	12.73	13.39	-
Corundum α-Al_2O_3	Rhombohedral	$D_{2}^{6}h$	2	4.758		12.991	-
Al_2O	Cubic	-	-	4.98	-	-	-
AlO· Al_2O_3	Cubic (spinel)	O_{h}^{7}	-	5.67	-	-	-
Beta aluminas							
Na_2O·$11Al_2O_3$	Hexagonal	$D_{2}^{4}h$	1	5.58	-	22.45	-
K_2O·$11Al_2O_3$	Hexagonal	$D_{2}^{4}h$	1	5.58	-	22.67	-
MgO·$11Al_2O_3$	Hexagonal	$D_{2}^{4}h$	1	5.56	-	22.55	-
CaO·$6Al_2O_3$	Hexagonal	$D_{2}^{4}h$	2	5.54	-	21.83	-
SrO·$6Al_2O_3$	Hexagonal	$D_{2}^{4}h$	2	5.56	-	21.95	-
BaO·$6AlO$	Hexagonal	$D_{2}^{4}h$	2	5.58	-	22.67	-
Zeta alumina							
Li_2O·$5Al_2O_3$	Cubic	O_{h}^{7}	2	7.90	-	-	-

2.2.2 Alpha alumina [47]

Aluminum oxide, or alumina, crystallizes in the corundum structure (mineralogical term) to form sapphire monocrystals. We are referring here to white sapphire, like the one used for the manufacture of scratchproof "glasses" for watches, whereas in gemmology sapphire is the blue sapphire, which is alumina with a little Ti4^{+}; ruby being alumina colored in red by Cr3^{+}. This is the alpha variety (α-Al_2O_3), which is the stable variety, but we will see that the preparation of alumina involves various metastable varieties: hydrated aluminas and transition aluminas.

The corundum structure belongs to the rhombohedric system, space group R$\bar{3}$c, the lattice parameters at room temperature being, in hexagonal axes, a = 0.4759 nm and c = 1.299 nm, with Z = 6. The crystal can be described as a compact hexagonal stacking of O^{2-}anions, in which the two-thirds of the octahedral interstices are occupied by Al^{3+} cations (see Figure 2.1). We note that this reference to anions and cations insists rather misleadingly on the ionicity of the bond: it is considered that the alumina bond is ionic for two-thirds and covalent for the remaining third part. The considerable amount of formation enthalpy (≈ 1,600 kJ mole^{-1}) which explains the absence of natural deposits of metal aluminum, makes alumina one of the most tightly bonded compounds, resulting in very high hardness (9 in the Mohs hardness scale, which goes from 1 (talc) to 10 (diamond), and where quartz is classified at 7) and high melting (2,050°C) and boiling temperatures (3,500°C). The density of sapphire is very close to 4 g.cm^{-3}, i.e. a little more than half the density of iron.

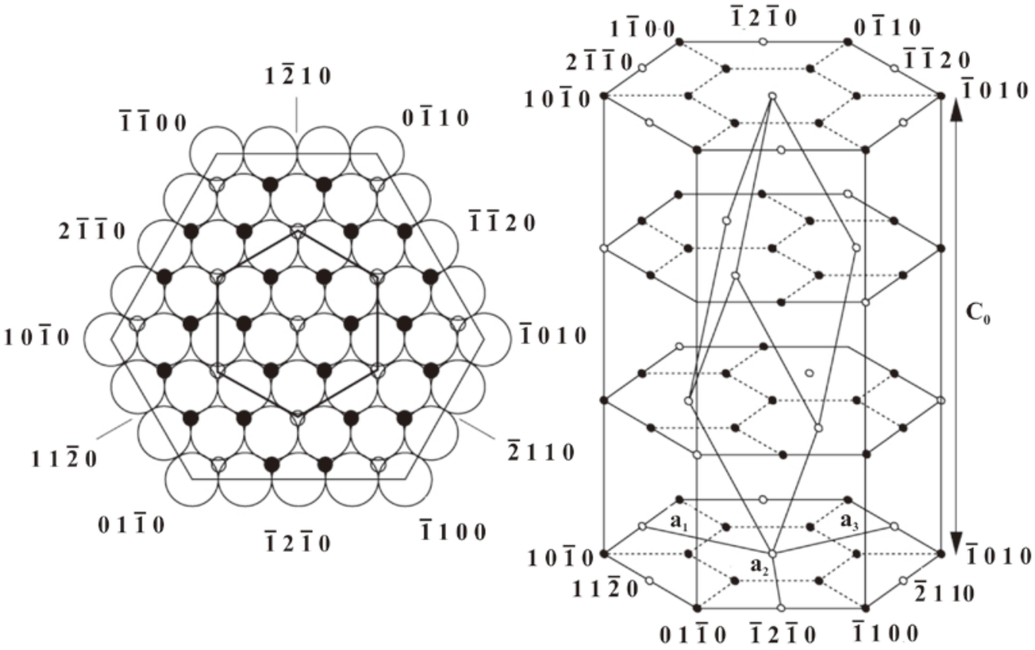

Figure 2.1 Structure of α alumina. On the left, seen in the base plan: the large circles represent the anions, the small full circles the cations, the small empty circles the vacant octahedral interstices. On the right, the view of the cation sublattice: the full circles represent the full cations and the circles the vacant sites [47]

2.3 Selected properties of alumina [48]

The selected properties of alumina are summarized in Table 2.3. The results must be viewed accordingly and some of these results and conclusions are still controversial.

Table 2.3 Selected properties of aluminas [48]

Properties	α-Al2O3	θ-Al2O3	γ-Al2O3
Density (kg/m^3)	3980	3560	3200
Elastic modulus (GPa)	409	441	-
Hardness (GPa)	28	-	-
Bulk modulus (GPa)	239	-	-
Band gap (eV)	8.8	7.4	-
Melting point (°C)	2051	θ → α (1050 °C)	γ → δ (700-800 °C)

2.4 Structural applications of alumina [47]

Alumina ceramics owe to the stability of this oxide and its strong atomic bonds their mechanical and thermal performances which imply but do not necessarily combined in a single type of microstructure high hardness, high modulus of elasticity, satisfactory mechanical strength, wear resistance and good tribological properties and refractarity. Giving accurate values would be useless because mechanical properties are sensitive properties which vary with the microstructure, and the hot properties depend highly on the temperature and chemical reactions when the environment is aggressive. To illustrate this point, a dense fine-grained alumina ceramic has a Young's modulus of ≈ 400 GPa (twice the modulus of steel), a Poisson's ratio of ≈ 0.25, a Vickers hardness of 20 GPa and a mechanical bending strength of ≈ 300 to 500 MPa. The mechanical strength being a value that expresses a particular sensitivity to measurement conditions . For high temperature applications, in the absence of corrosion, sintered alumina pieces allow long duration uses, at temperatures that can exceed 1,600°C, but at stress levels that should not exceed a few MPa.

Toughness at 20°C is equal to ≈ 3.5 MPa m$^{1/2}$ which is a respectable amount for a ceramic, but does not make alumina a tough material, especially when compared to metals. Ductility is modest. The coefficient of thermal expansion between 20°C and 1,000°C is 8.5×10^{-6} K^{-1}. This relatively high thermal expansion for a ceramic combines with a high Young's modulus in order to lower the first parameter of resistance to thermal shocks: alumina ceramics are not very resistant to thermal shocks. The expansion anisotropy is low (9×10^{-6} K^{-1}parallel to the ternary axis of the crystal and 8.3×10^{-6} K^{-1} perpendicular to this axis) and therefore the residual stresses at the grain boundaries are reduced. In order to complete the comment on a good resistance at high temperatures under weak mechanical load, it must be noted that we observe a poor creep resistance under substantial load. Alumina ceramics are best suited for mechanical uses (excluding shocks) or refractory uses, but they are not thermomechanical materials, if this word means combination of mechanical and thermal performances.

Table 2.4 illustrates the main applications of alumina powders, shows the desired properties and indicates the recommended powders.

Table 2.4 Recommendations for choosing alumina powders [49]

Applications	Main desired characteristics	Sodium content/reactivity
High voltage insulator	Mechanical and electric strength resistance to arc effects, purity, resistance to thermal shocks	Normal
Spark plugs	Mechanical and electric strength, controlled shrinkage, durability, green workability, resistance to thermal shocks	Normal to low
Ceramics for electronics	Resistance to high temperatures, high electric resistance, thermal conductivity, ease of metallization	Low
Tiles, enamels	Mechanical and chemical properties, controlled fusion and viscosity, adjustment of surface effects	Intermediate
Metallized substrates	Good thermal conductibility, ease of metallization	Low/reactive
Catalysis support	Preparation of cordierite, thermal conductivity, surface control	Normal
Ceramic filters for molten metal	Surface control, good thermal conductivity, resistance to thermal shocks	Normal
Crockery, sanitary	Mechanical and chemical resistance, whiteness	Normal
Ceramics for mechanics	Mechanical resistance, thermal conductivity, resistance to corrosion, abrasion and thermal shocks	Normal to weak/reactive
Tribology	Uniform microstructure, compromise between hardness and toughness	Normal

2.5 Pulse forming network [49]

Flashlamps are usually operated from a single or multiple-mesh LC network. The network stores the discharge energy and delivers it to the lamp in the desired current pulse shape. In most situations, the lamp input energy E_0, the pulse width T_p and the lamp dimensions have been determined before the Pulse Forming Network is designed.

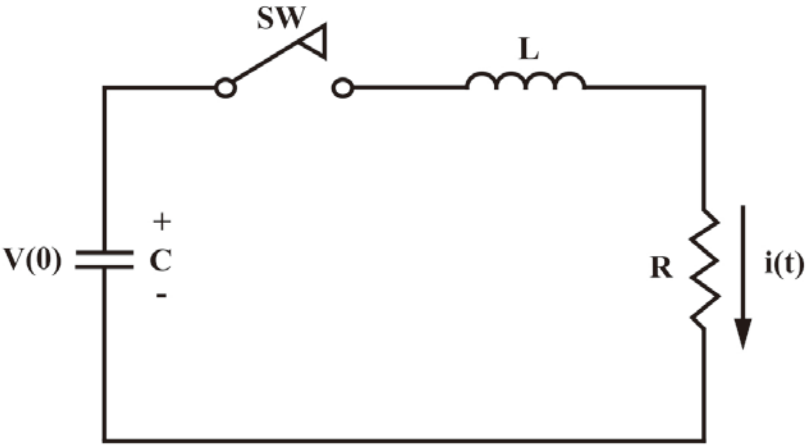

Figure 2.2 Single-mesh discharge circuit

The above-mentioned parameters completely describe the network's capacitance and inductance as well as the charging voltage and peak current. To familiarize the reader with the design of flashlamp energy-storage networks, we will consider first the elementary model of a pulse discharge circuit (Figure 2.2). The capacitor C is charged to an initial voltage V_0. At time t = 0 the switch SW is closed and the energy stored in the capacitor is delivered to the load. We assume for the moment that the load is a linear resistor R. In this case the circuit is described by the second order of differential equation.

$$\frac{d^2i(t)}{dt^2} + 2\alpha\frac{di(t)}{dt} + \omega^2 i(t) = 0 \tag{2.1}$$

$$\alpha = \frac{R}{2L},\ \omega = \frac{1}{\sqrt{LC}} \text{ and } \zeta = \frac{\alpha}{\omega},\ \zeta = \frac{R}{2}\sqrt{\frac{C}{L}}$$

Under damped ($\zeta < 1$), overdamped ($\zeta > 1$) and critically damped ($\zeta = 1$)

$$s^2 + 2\alpha s + \omega^2 = 0 \tag{2.2}$$

$$s_1 = -\alpha + \sqrt{\alpha^2 - \omega^2}$$

$$s_2 = -\alpha - \sqrt{\alpha^2 - \omega^2}$$

$$i(t) = A_1 e^{s_1 t} + A_2 e^{s_2 t} \tag{2.3}$$

Overdamped response
The overdamped response ($\zeta > 1$) is

$$i(t) = A_1 e^{-\omega(\zeta + \sqrt{\zeta^2 - 1})t} + A_2 e^{-\omega(\zeta - \sqrt{\zeta^2 - 1})t} \tag{2.4}$$

The underdamped response ($\zeta < 1$) is

$$i(t) = B_3 e^{-\alpha t} \sin(\omega_d t + \varphi) \tag{2.5}$$

$$\omega_d = \sqrt{\omega^2 - \alpha^2} = \omega\sqrt{1-\zeta^2}$$

Critically damped response
The critically damped response ($\zeta = 1$) is

$$i(t) = D_1 t e^{-\alpha t} + D_2 e^{-\alpha t} \tag{2.6}$$

2.6 Laser materials interactions [50]

Laser radiation is essentially electromagnetic wave, associated with electric ($\vec{E}$) and magnetic field vectors ($\vec{H}$). Absorption of light can be explained as the interaction of the electromagnetic radiation (characterized by electric and magnetic vectors) with the electrons (either free or bound) of the material. Electromagnetic radiation can interact only with the electrons of the atoms of the material because the much heavier nuclei are not able to follow the high frequencies of laser radiation. When the electromagnetic radiation passes over the electrons it exerts a force and sets the electrons into motion by the electric field of the radiation. The force exerted by the electromagnetic radiation of the electron can be expressed as

$$\vec{F} = e\vec{E} + e\left(\frac{v}{c} \times \vec{H}\right) \tag{2.7}$$

where v is the velocity of electron and c is the speed of light. If it is considered that the electric and magnetic field carry the same amount of energy, then, according to above equation, the contribution of magnetic field to the force is smaller than that of the electric field by a factor of the order of v/c. Hence, the most important term in the above equation is $e\vec{E}$. The absorbed radiation, thus, results in the excess energy of the charged particles such as kinetic energy of the free electrons, excitation energy of the bound electrons, etc. Eventually, the degradation of the ordered and localized primary excitation energy through various steps leads to the generation of heat. Hence, the absorption process is sometimes referred to as the secondary “source” of energy inside the material and is used to determine the extent of various effects on the material during laser–material interactions.

The absorption of laser radiation in the material is generally expressed in terms of the Beer-Lambert law:

$$I(z) = I_0 e^{-\mu x} \tag{2.8}$$

where I_0 is the incident intensity, I(z) is the intensity at depth z, and µ is the absorption coefficient. Thus, the intensity of the laser radiation gets attenuated inside the material. The length over which the significant attenuation of laser radiation takes place is often referred to as the attenuation length and is given by the reciprocal of the absorption coefficient :

$$L = \frac{1}{\mu} \tag{2.9}$$

For a strongly absorbing material, the absorption coefficients are in the range of 10^5–10^6 cm^{-1} such that the attenuation lengths are in the range 10^{-5}–10^{-6} cm.

One of the important parameters influencing the effects of laser–material interactions is the absorptivity of the material for laser radiation. It can be defined as the fraction of incident radiation that is absorbed at normal incidence. For opaque materials, the absorptivity (A) can be expressed as :

$$A = 1 - R \tag{2.10}$$

where R is the reflectivity of the material. The reflectivity and the absorptivity of the material can be calculated from the measurements of optical constants or the complex refractive index. The complex refractive index (n_c) is defined as:

$$n_c = n - ik \tag{2.11}$$

where n and k are the refractive index and extinction coefficient, respectively These parameters are strong functions of wavelength and temperature. The reflectivity at normal incidence is then defined as:

$$R = \frac{(n-1)^2 + k^2}{(n+1)^2 + k^2} \tag{2.12}$$

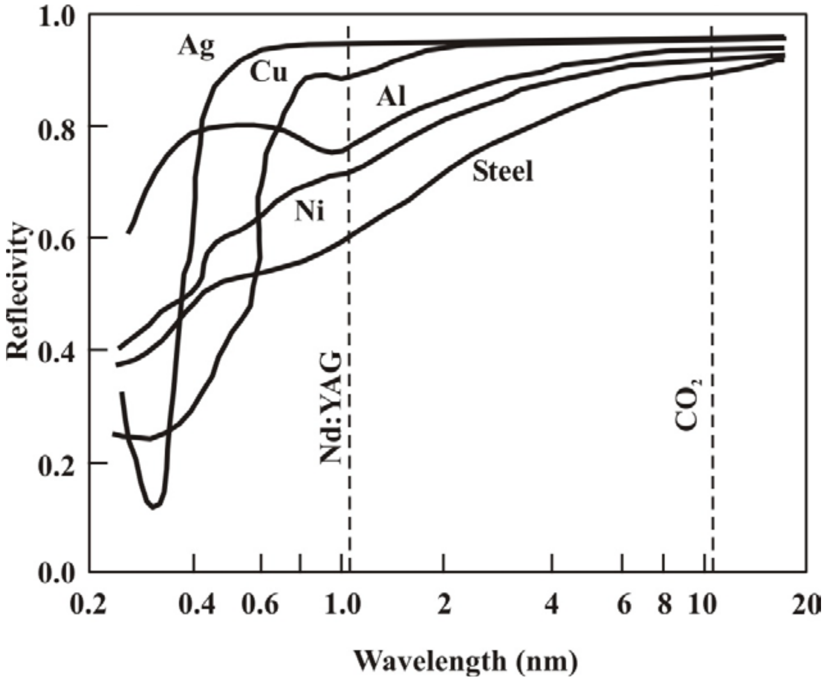

Figure 2.3 Variation of reflectivity with wavelength for several metallic materials. The wavelengths of two important lasers (Nd:YAG and CO_2) are superimposed on the figure [51]

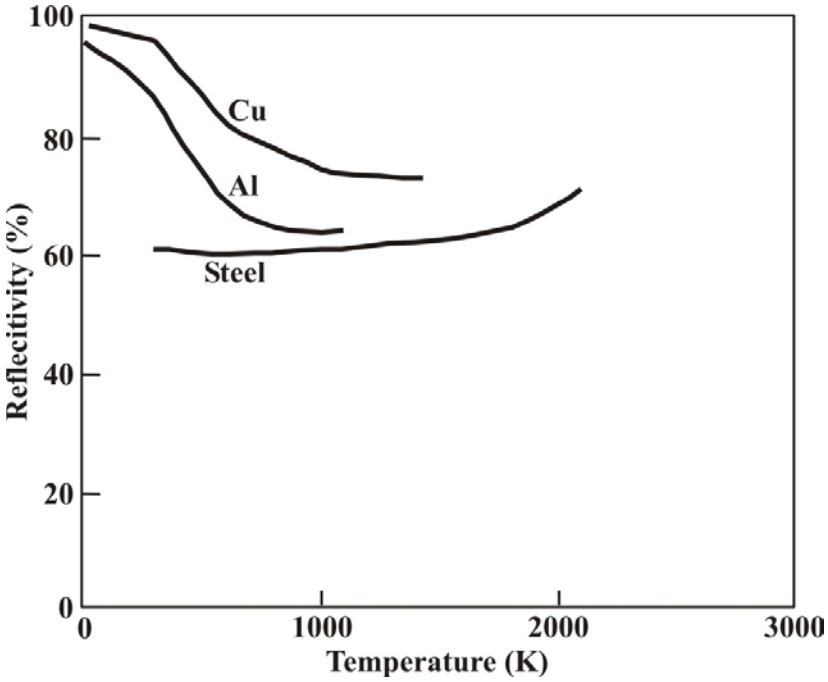

Figure 2.4 Variation of reflectivity with temperature for 1.06 μm radiation [51]

Since parameters *n* and *k* are strong functions of wavelength and temperature, the reflectivity (and hence the absorptivity) of the material is greatly influenced by the wavelength and temperature.

The variation of reflectivity with the wavelength of some common metallic materials is presented in figure 2.3. The wavelengths of two important lasers (Nd:YAG and CO_2) are superimposed on the figure. As indicated in the figure, the reflectivity of the material generally increases with increasing wavelength. Thus, the materials are strong absorbers (less reflective) at shorter wavelengths. For a given material, the radiation from Nd:YAG laser (λ = 1.064 μm) is absorbed strongly than the CO_2 laser (λ = 10.6 μm). However, such wavelength dependence of the reflectivity (and hence absorptivity) should be used only as guidelines because there are several other factors which may strongly influence the absorptivity. For example, the reflectivity of a material generally decreases with increasing temperature (figure 2.4). Hence, a material which is strongly reflective at low temperature may become strongly absorbing at high temperature. This is of particular importance in the laser processing of materials where laser–materials interaction results in significant increase in the surface temperatures. Other parameters which influence the absorptivity of the material include angle of incidence of the radiation and surface condition of the material. These concepts have been extensively utilized to improve the coupling of the laser radiation to the reflective material by applying antireflective surface coatings and laser irradiating the material at suitable angle of incidence.

The laser energy absorbed by the material during laser-material interaction is converted into heat by degradation of the ordered and localized primary excitation energy. The typical overall energy relaxation times are of the order of 10^{-13} s for metals (10^{-12}-10^{-6} s for nonmetals). The conversion of light energy into heat and its subsequent conduction into the material establishes the temperature distributions in the material. Depending on the magnitude of the temperature rise, various physical effects in the material include heating, melting, and vaporization of the material. Furthermore, the ionization of vapor during laser irradiation may lead to generation of plasma. In addition to the thermal effects, the laser–material interactions may be associated with photochemical processes such as photoablation of the material. These effects of laser–material interactions are schematically presented in figure 2.5.

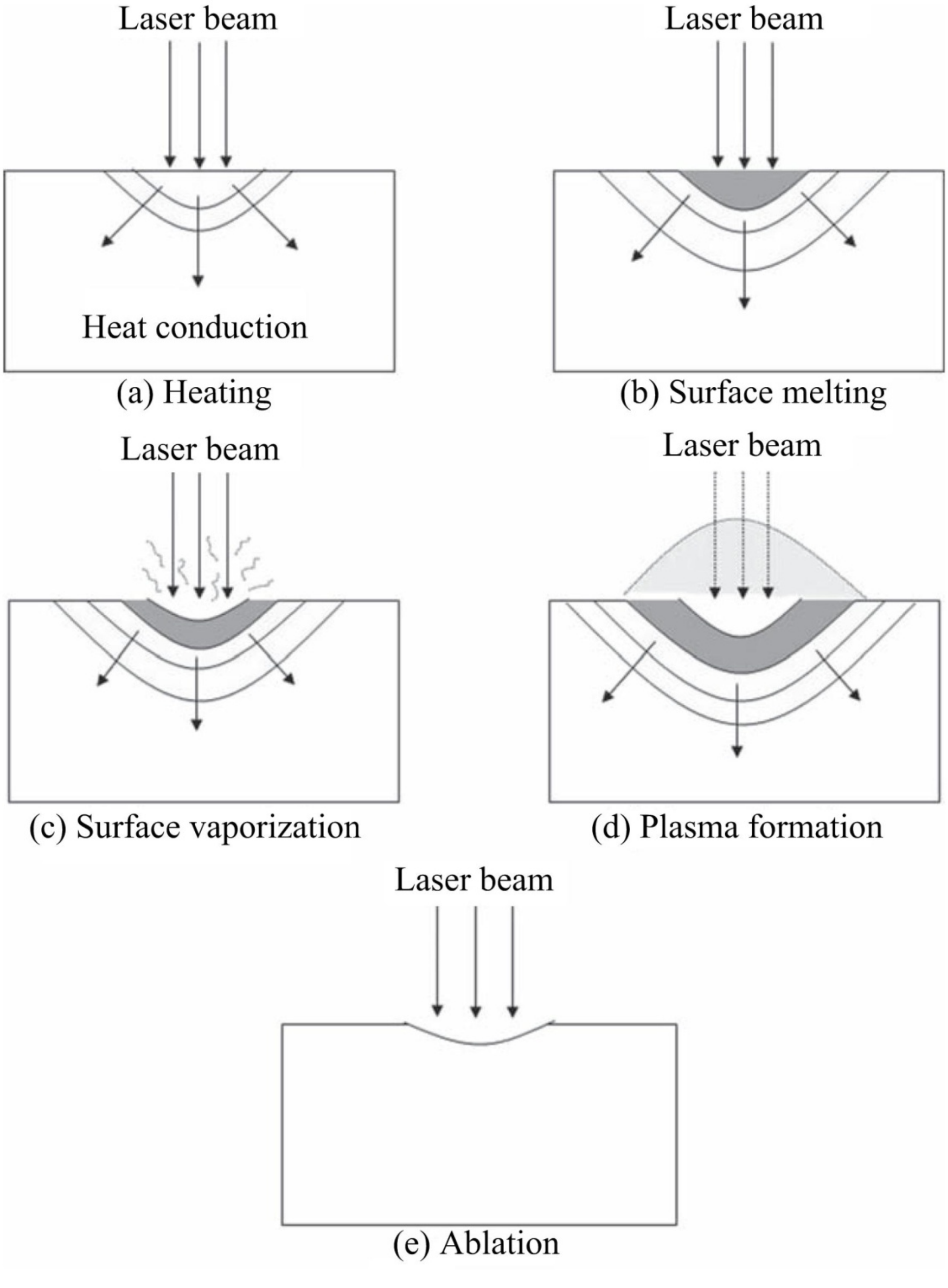

(a) Heating

(b) Surface melting

(c) Surface vaporization

(d) Plasma formation

(e) Ablation

Figure 2.5 Various effects of laser–material interaction (a) heating, (b) surface melting, (c) surface vaporization, (d) plasma formation, and (e) ablation [51].

All of these effects play important roles during laser materials processing. There exist distinct combinations of laser intensities and interaction times where specific effect of laser–material interaction dominates. Figure 2.6 presents one such plot showing the regimes of various laser–material interactions and their applications in materials processing.

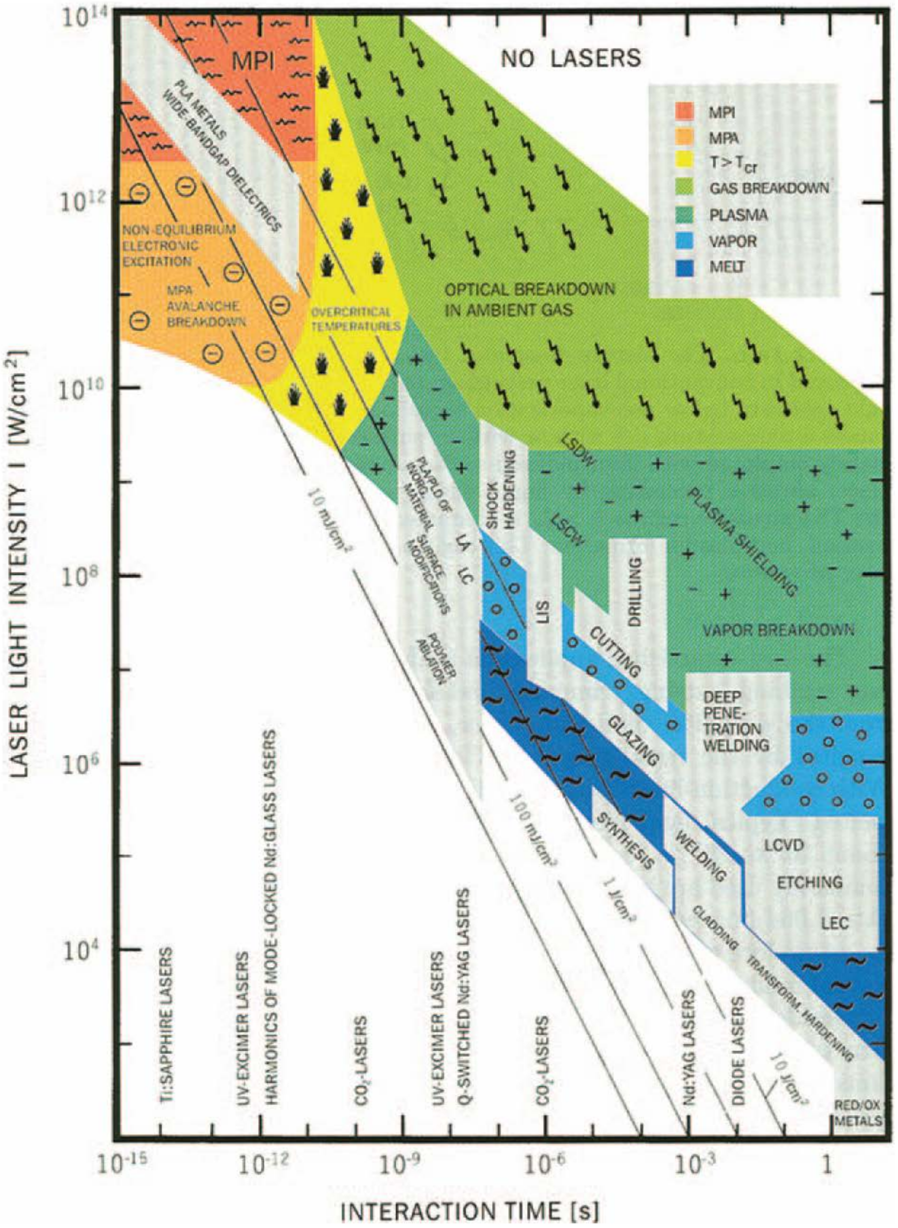

Figure 2.6 Regimes of various effects during laser–material interactions and their application in laser materials processing (pulsed laser ablation/deposition, PLA/PLD; laser annealing, LA; laser cleaning, LC; laser-induced isotope separation, LIS; multiphoton absorption/ionization, MPA/ MPI; laser-supported detonation/combustion waves, LSDW/LSCW; laser-induced CVD, LCVD; laser-induced electrochemical plating/etching, LEC; long pulse or CW CO_2 laser-induced reduction/oxidation, RED/OX [51].

2.7 Thermal Effects [50]

When a laser beam of intensity I_0 is irradiated on the surface of material, it results in the excitation of free electrons (in metals), vibrations (in insulators), or both (in semiconductors). As mentioned in the previous section, this excitation energy is rapidly converted into heat (time duration in the range 10^{-13} s for metals, 10^{-12} to 10^{-6} s for nonmetals). This is followed by various heat transfer processes such as conduction into the materials, and convection and radiation from the surface. The most significant heat transfer process being the heat conduction into the material. The generation of heat at the surface and its conduction into the material establishes the temperature distributions in the material depending on the thermo-physical properties of the material and laser parameters. If the incident laser intensity is sufficiently high, the absorption of laser energy can result in the phase transformations such as surface melting and evaporation. Generally, these phase transformations are associated with threshold (minimum) laser intensities referred to as melting and evaporation thresholds (I_m and I_v). Melting and evaporation are the efficient material removal mechanisms during many machining processes. In this section, we will deal with the simplified analysis of laser heating, melting, and evaporation of materials. More detailed analyses are presented in the following chapters with reference to specific applications.

2.7.1 Heating

To understand the effects of laser irradiation on the material, it is necessary to evaluate the temporal and spatial variation of temperature distribution. The most simplified thermal analysis is based on the solution of one-dimensional heat conduction equation with simplified assumptions such as

1. Material is homogeneous. The thermo-physical properties are independent of temperature.
2. The initial temperature of the material is constant.
3. Heat input is uniform during the irradiation time.
4. The convection and radiation losses from the surface are negligible.

The schematic geometry of laser irradiation and corresponding temperature profiles during laser heating are presented in Figure 2.7. The governing equation for the one dimensional heat transfer can be written as:

$$\frac{\partial T(z,t)}{\partial t} = \alpha \frac{\partial^2 T(z,t)}{\partial z^2} \tag{2.13}$$

where T is the temperature at location z, after time t; and α is the thermal diffusivity.

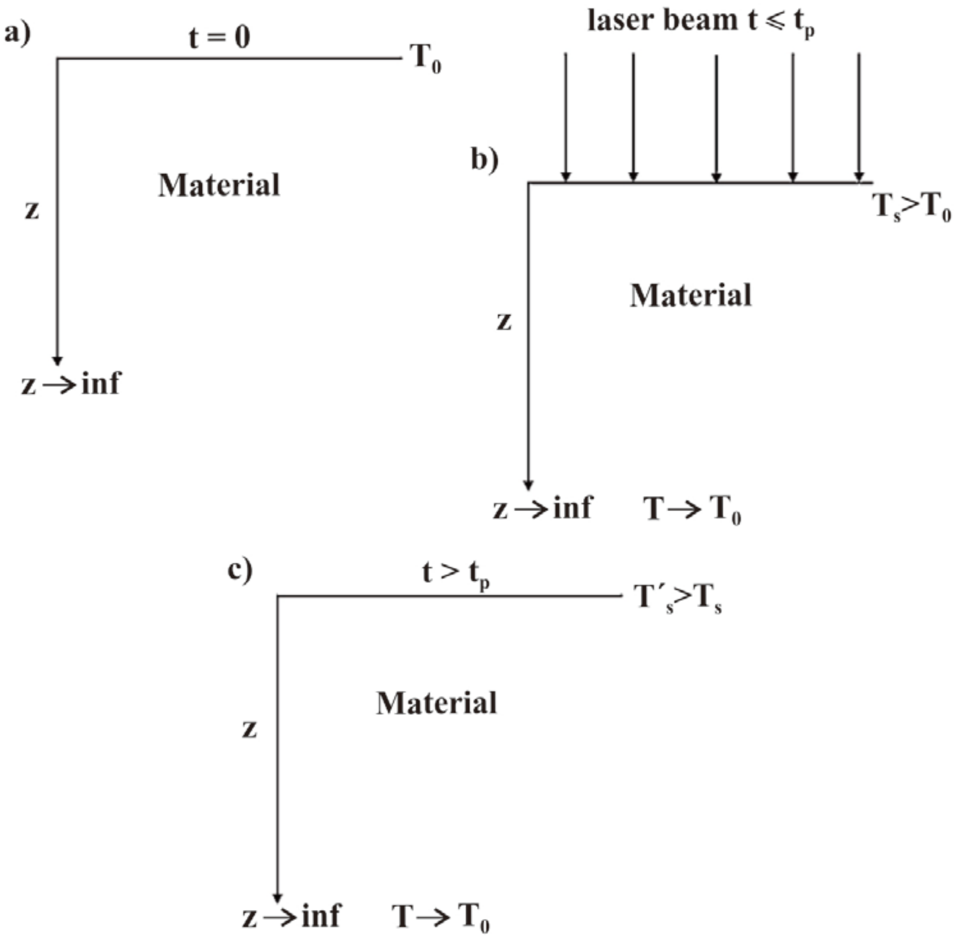

Fig. 2.7 Schematic of the laser irradiation geometry and surface temperatures at various times: (a) initial condition with uniform temperature T_0, throughoutthe material, (b) laser heating with surface temperature, $T_s > T_0$, and **(c)**cooling stage (laser off) with surface temperature $T'_s < T_s$ (surface temperatures are less than melting point at all times)[51]

The initial condition can be written as:

$$T(z,0) - T_0, \text{for } 0 \leq z \leq \infty, t = 0 \tag{2.14}$$

where T_0 is the initial constant temperature of the material. The simple boundary condition at the surface ($z = 0$) assuming that laser energy absorbed at the surface equals the energy conducted can be written as:

$$-k \frac{\partial T(0,t)}{\partial z} = \delta H \tag{2.15}$$

where k is the thermal conductivity and H is the absorbed laser energy. The absorbed laser energy H can be given by the product of absorptivity A and incident laser power density I_0(i.e., $H = AI_0$). If t_p is the irradiation time (pulse on time) then the parameter *d* equals unity when the laser is on, i.e., $0 \leq t \leq t_p$. It can be taken as zero when the laser is off, i.e., $t > t_p$. The solutions of these equations can be obtained as follows:

During heating ($0 < t < t_p$):

$$\Delta T(z,t)_{t<t_p} = \frac{H}{k}(4\alpha t)^{1/2}\,\mathrm{ierf}\left(\frac{z}{(4\alpha t)^{1/2}}\right) \tag{2.16}$$

During cooling ($t > t_p$):

$$\Delta T(z,t)_{t>t_p} = \frac{2H\alpha^{1/2}}{k}\left[t^{1/2}\,\mathrm{ierf}\left(\frac{z}{(4\alpha t)^{1/2}}\right) - (t-t_p)^{1/2}\,\mathrm{ierf}\left(\frac{z}{(4\alpha(t-t_p))^{1/2}}\right)\right] \tag{2.17}$$

The function ierfc(x) is defined as:

$$\mathrm{ierfc}(x) = \frac{1}{\pi}\left\{\exp(-x^2) - x(1-\mathrm{erf}(x))\right\}$$

where $\mathrm{erf}(x) = \frac{2}{\pi}\int_0^x e^{\zeta^2}\,d\zeta$

The temperature at the surface during heating and cooling can be obtained by substituting z = 0 in Eqs (2.10) and (2.11). Thus

$$\Delta T(0,t)_{t<t_p} = \frac{H}{k}\left(\frac{4\alpha t}{\pi}\right)^{1/2} \tag{2.18}$$

$$\Delta T(0,t)_{t>t_p} = \frac{H}{k}\left[\left(\frac{4\alpha t}{\pi}\right)^{1/2} - \left(\frac{4\alpha(t-t_p)}{\pi}\right)^{1/2}\right] \tag{2.19}$$

Typical calculated temperature changes at various depths during laser irradiation of copper using laser power density of 10^{10} W/m^2 and irradiation time of 1 μs are presented in Figure 2.8. The important characteristics of the temperature changes in a material during laser irradiation can be listed as

1. At the surface (z = 0), the temperature increases with increasing irradiation time, reaches maximum corresponding to pulse time (t_p), and then rapidly decreases. Thus, the heating and the cooling parts of the curve are clearly separated at a time corresponding to pulse time.
2. At certain depths below the surface (z > 0), the temperature increases with increasing irradiation time, reaches maximum, and then decreases. However, the maximum temperature does not reach exactly at the pulse time (t_p), but at the longer time ($t > t_p$). The time ($t > t_p$) to reach the maximum temperature increases as we go further into the depth below the surface of the material.

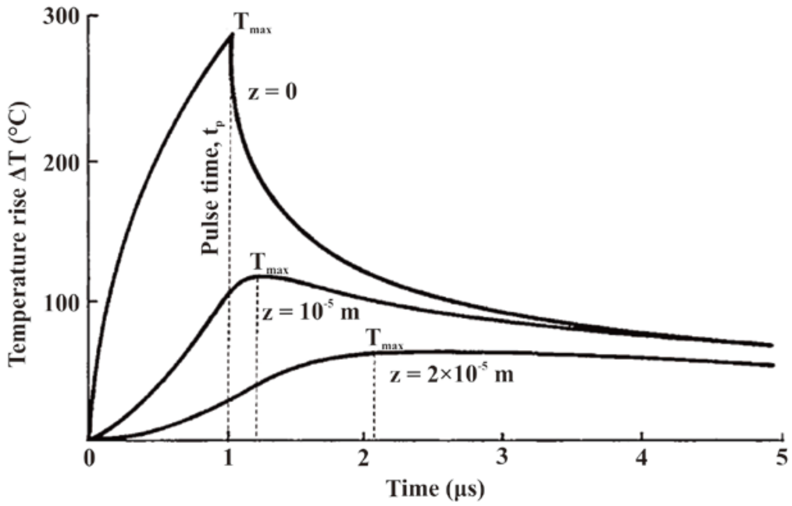

Figure 2.8 Variation of calculated temperature increases with time at various depths during laser irradiation of copper using laser power density of 10^{10} W/m^2 and irradiation time of 1 μs [51]

2.8 Laser ablation [50]

The ablation during laser processing refers to the material removal due to thermal and/or photochemical (nonthermal) interactions. The laser–material interactions during ablation are complex and may involve the interplay between thermal and photochemical processes often referred to as photophysical processes. Figure 2.9 presents the various mechanisms of laser ablation.

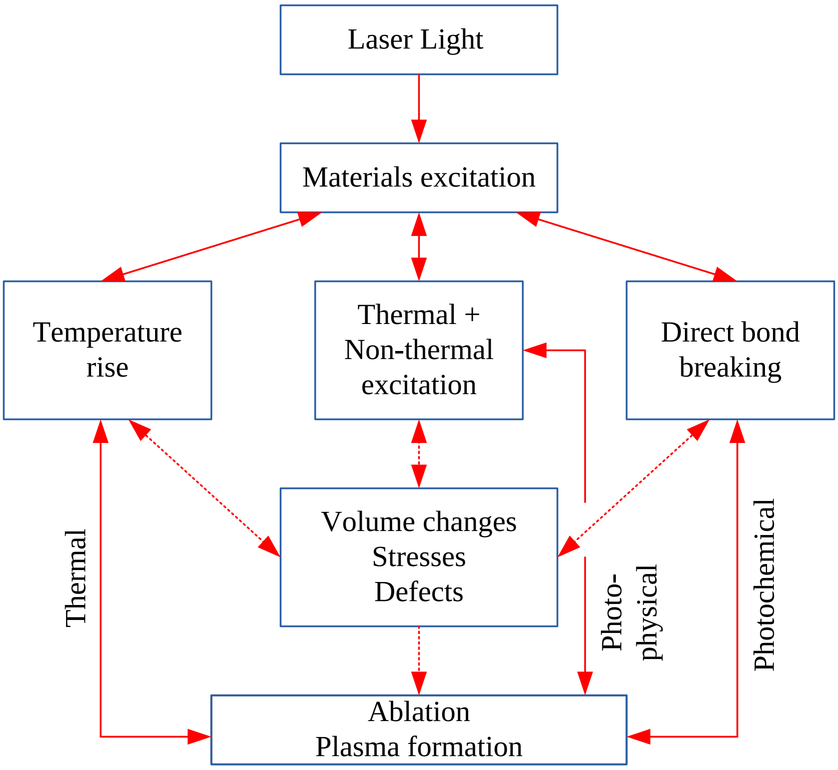

Figure 2.9 Various mechanisms of laser ablation [51]

2.9 Laser ablation in liquid [51]

The process of laser ablation of solids in liquids has attracted much attention of researchers during the last decade. This is due mainly to the simplicity of the experimental setup. Many modern laboratories (and not only physical ones) are equipped with lasers, and synthesis of nanoparticles is a strong temptation. The process proceeds in one step and results in immediate formation of nanoparticles in the liquid in which the target is immersed. The main feature of the process is that ideally the liquid contains only nanoparticles made of the target material and the liquid. There are no counter-ions or residuals of reducing agents left in the solution. For this reason laser ablation of solids in liquids can be considered as a method of nanoparticle synthesis, which is an alternative to chemical methods.

Commercially available laser sources are characterized by a number of parameters, such as peak power, average power, wavelength of emission, pulse repetition rate, etc. If the final purpose of ablation of a target immersed into a liquid is the synthesis of nanoparticles with desired properties, such as their chemical composition, size distribution, concentration, etc., then the above mentioned laser parameters are of different importance to the properties of desired nanoparticles. Also, the nature of the liquid plays a significant role in the final properties of nanoparticles generated under laser ablation.

2.9.1 General setup of laser ablation in liquids

Figure 2.10 shows a generalized setup of experiments on laser ablation of solids in a liquid environment. This setup may vary from one research group to another, though their common features are the same.

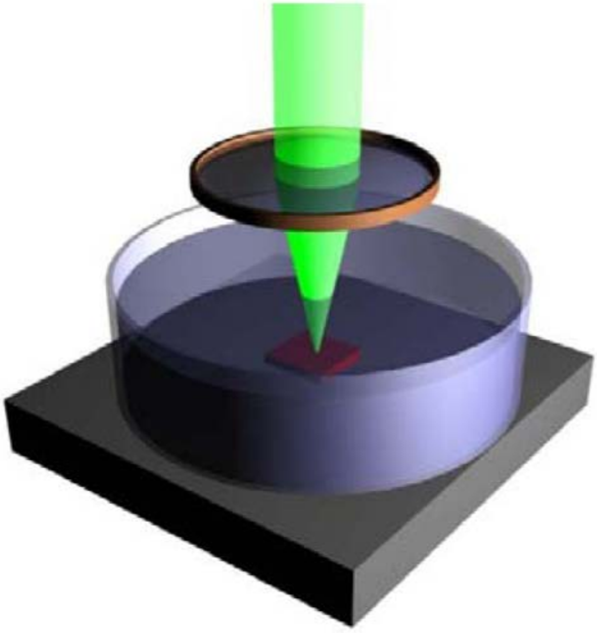

Figure 2.10 Experimental setup for laser ablation of solids in a liquid environment[52]

Laser radiation is focused onto a solid target immersed in a liquid. It is assumed that the liquid is transparent at the laser wavelength, otherwise the focalization of the beam would be problematic due to absorption of laser radiation in it. The simplest way is working with the free surface of the liquid, which allows avoiding additional reflection at the interface “covering glass/air”. However, the use of volatile liquids, such as acetone, ethanol, etc., requires covering the liquid with a window that is transparent at the laser wavelength.

2.9.2 Experimental technique

The experimental setup for laser ablation in a liquid environment is perfectly simple. It is usually assumed that the liquid that surrounds the solid target is transparent at laser wavelength while the laser radiation is absorbed by the target. A solid target is placed under a thin (several millimeters) layer of liquid and is exposed to laser radiation through this layer. Different pulsed laser sources can be used, e.g., a Nd:YAG laser at 1.06 μm output and its harmonics, a Cu vapor laser, a Ti:sapphire laser, etc. UV excimer lasers are less common, since most liquids and NP absorb in the UV region. The only necessary requirement is that the laser beam is sufficiently powerful to induce local melting of the target. Usually the laser beam is focused onto the target using an appropriate optics to a certain size of laser spot (see figure 2.10). In some experiments the target is rotated under the laser beam to avoid the exposure of the same area. Some research uses a sealed-off cell to avoid oxidation of nanoparticles by air oxygen, but basically the setup is the same. It is the density of the laser energy (in J/cm^2), or so-called fluence, that determines the temperature of the target and the possibility to produce surface melting and eventual generation of nanoparticles. The irradiation of the metal surface results in fast removal of the material that is confined to the laser spot. The ejected nanoparticles remain in the liquid that surrounds the target, resulting in formation of a so called colloidal solution. Unlike real solutions that contain ionic or molecular species, colloidal solutions also contain particles, e.g., nanoparticles and clusters. Due to accumulation of nanoparticles in the surrounding liquid, their prolonged interaction with laser radiation is possible. Therefore, the thickness of the liquid layer above the target is also an important experimental parameter that may influence the properties of generated nanoparticles. Different laser parameters are of different importance to the efficiency of nanoparticles generation.

2.9.3 Pulse duration

Usually, pulsed laser sources are used for generation of nanoparticles in liquids with pulse duration from hundreds of femtoseconds to hundreds of nanoseconds. The nanoparticles under laser ablation in liquids are formed owing to sputtering of the molten layer by the recoil pressure of the liquid that surrounds the target. Therefore, the necessary condition of nanoparticles synthesis is melting of the target material. In general, the temperature distribution under laser exposure of solids can be found solving a heat conduction equation with corresponding boundary conditions. However, in the case of short laser pulses of the duration mentioned above, the complicated problem of temperature calculation can be significantly simplified. This simplification is based on the fact that the heat diffusion length l_d from laser-exposed areas of the target during the duration of the laser pulse t_p is small compared to laser spot size d. Indeed, in a typical experiment on pulsed laser ablation d ~ 10 μm, while the heat diffusion length is much less. Assuming that the laser beam has a flat-top profile (typical of excimer lasers, metal vapor lasers, etc.) one may suggest that the absorbed laser energy is spent for heating of the target layer whose thickness is of order of $(at_p)^{1/2}$, where a stands for the heat diffusion coefficient of the target material, while the area of this layer coincides with the laser spot. Unlike to what one might believe, the presence of liquid around the target does not alter noticeably the temperature inside the laser spot. The reason is that the heat diffusion coefficient for liquids is even smaller than that of solids. Presence of the liquid may affect only the average temperature rise of the target if the repetition rate of laser pulses is elevated, e.g., of order of 1 kHz and more. Simple heat balance equation leads for the following expression of the temperature T within the laser spot:

$$T \approx \frac{Aj}{c\rho h} \tag{2.20}$$

where A stands for absorptivity of the target at the laser wavelength, A = 1- R, where R is the reflectivity coefficient at laser wavelength, c stands for heat capacity of the target material, ρ is density of the target material, and h is the heat diffusion length inside the target. One can see that in a quite natural way the temperature is proportional to the energy density of the laser beam, or so called fluence j. The heat diffusion length h depends on the heat diffusivity of the target material:

$$h \propto \sqrt{at_p} \tag{2.21}$$

where in turn $a = k/c\rho$, where k is the heat conduction coefficient of the target, and t_p stands for laser pulse duration. The longer is the laser pulse t_p, the thicker is the layer of the material which is heated by absorbed laser energy. The above made estimation of the temperature rise T is made assuming superficial absorption of laser radiation. If α is the coefficient of absorption of laser radiation, then this condition can be written as follows:

$$\alpha^{-1} << h \tag{2.22}$$

Of course some energy is consumed for heating and evaporation of a liquid adjacent to the laser spot, but this energy is small compared to the absorbed one due to low thermal conductivity of liquids

In case of metal targets laser radiation is absorbed by free electrons that transfer their energy to the metal lattice within 3- 5 picoseconds. Virtually no heat exchange with the bulk of the solid target occurs, and the absorbed laser energy is spent for heating of the layer within the absorption depth α^{-1} of laser radiation.

The absorptivity A of the target surface is a complex parameter. For a smooth metallic surface it can be calculated using reference data on both real and imaginary part of a complex dielectric function of the material. However, as soon as the surface of the target is not flat and is characterized by a certain relief, the absorptivity of the target may largely deviate from its theoretical value. This is due to the dependence of absorptivity on the angle of incidence of radiation. Since the target material is dispersed into surrounding liquid as nanoparticles during laser ablation in liquids, the formation of the relief indeed occurs.

2.9.4 Laser wavelength

As soon as laser ablation of metals is considered, any wavelength is appropriate.
However, laser radiation can be absorbed by nanoparticles that are generated under ablation of the target. The majority of nanoparticles absorb in UV region, which imposes certain drawback on the use of excimer UV lasers for generation of nanoparticles.

2.9.5 Repetition Rate

Nanoparticles are ejected from the solid target at each pulse provided that the absorbed laser energy is sufficient to melt it. Therefore, the higher is the repetition rate of laser pulses, the higher is the rate of nanoparticles generation. However at high repetition rate the target may be screened from the beam by gas bubbles that have remained from previous pulses. This can be avoided using either a flow cell or elevated velocity of scanning (rotation) of the target.

2.10 Characterization method

2.10.1 Scanning electron microscopy (SEM) [52]

The principle of a scanning electron microscope (SEM) is shown schematically in figure 2.11. The two major parts are the microscope column and the electronics console. The microscope column consists of the electron gun (with the components cathode, Wehnelt cylinder, anode), one or two condenser lenses, two pairs of beam deflection coils (scan coils for X, Y deflection), the objective lens, and some apertures. In the specimen chamber at the lower end of the microscope column are located the specimen stage and the detectors for the different signals generated by the electron–specimen interaction. The microscope column and the specimen chamber are evacuated using a combination of prevacuum and high vacuum pumps (usually oil diffusion pumps). The pressure in the specimen chamber typically amounts to about 10^{-4} Pa, allowing the beam electrons to travel from the cathode to the specimen with little interaction with the residual gas molecules. The electronics console consists of the electric power supplies for the acceleration voltage (usual range about 0.5–30 kV) as well as the condenser and objective lenses, the scan generator, and electronic amplifiers for the different signals acquired. Moreover, the console also houses one or more monitors [cathode ray tube (CRT) or liquid crystal display (LCD)] for displaying the micrograph(s), a photo-CRT for analogous image recording, and numerous knobs and a computer keyboard to control the electron beam, the signals selected, and the image recording. Now modern SEMs mostly use a PC to control the electron beam, to select the signals, and to record as well as to store the digital image(s). In that case the numerous knobs are obsolete and are replaced by a mouse-controlled interactive program running on the PC.

The beam electrons are emitted from the cathode and accelerated by a voltage of 0.5–30 kV between the cathode and anode forming a smallest beam cross section—the crossover—near the anode with a diameter of about 10–50 µm. This spot size is too large to produce a sharp image. Therefore the crossover is demagnified by the lens system consisting of one or two condenser lenses and one objective lens and focused on the specimen surface. Most SEMs can produce an electron beam having a smallest spot size of about 5–10 nm and an electron probe current in the range of 10^{-12} - 10^{-10} A, which is sufficient to form an image with a reasonable signal-to-noise (S/N) ratio. For higher probe currents required for some modes of operation the smallest probe spot size increases to 100 nm or more. The objective lens has a variable relatively long focal length that allows a large working distance (WD; it corresponds to the distance between the specimen and lower pole piece) in the range of about 5–30 mm. This ensures that the various signals generated by the impinging beam electrons (figure 2.12) in the small specimen interaction volume can be collected by detectors located lateral above the specimen with sufficient efficiency. Pairs of beam deflection coils located in front of the objective lens and controlled by a scan generator scan the electron probe line by line across a small area of the specimen. Simultaneously, the scan generator controls the deflection coil system of a monitor. The intensity of the monitor is modulated by the amplified signal selected by the operator.

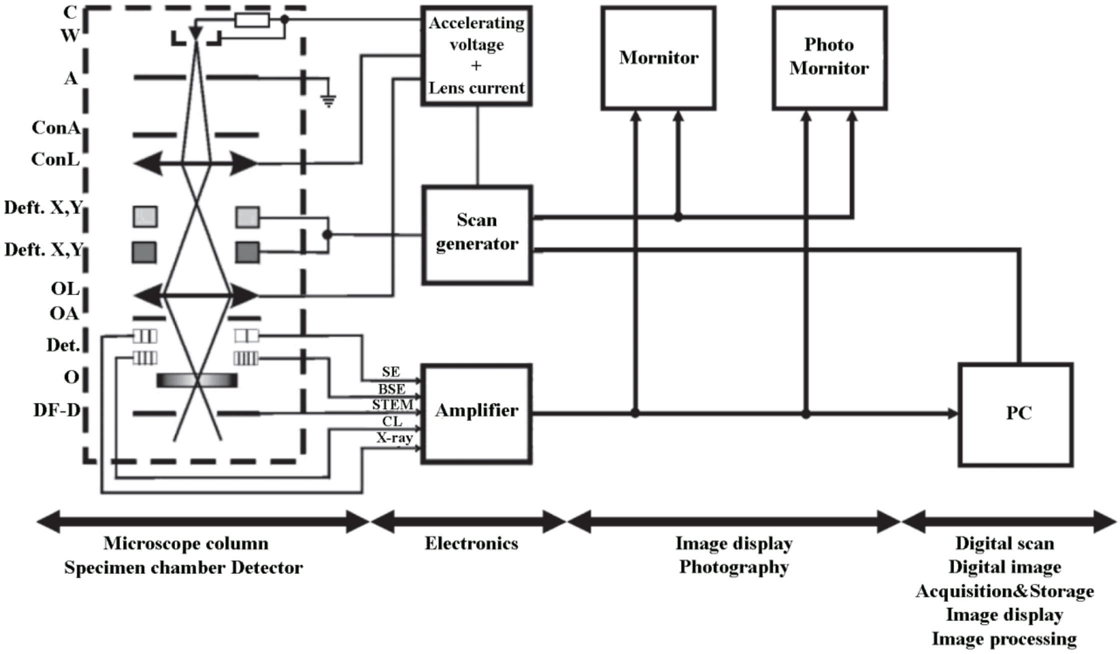

Figure 2.11 Schematic drawing of a conventional SEM. The evacuated microscope column (inside the bold dashed frame) contains the electron gun, electromagnetic lenses, electromagnetic deflection coils, apertures, the specimen stage, and the detectors. The electronics console houses the power supplies for the acceleration voltage and the electromagnetic lenses, the scan generator, amplifiers for the signals, and monitors for display and recording of images. Modern SEMs are controlled by a PC. A, anode; BSE, backscattered electrons; C, cathode; ConA, condenser aperture; ConL, condenser lens; CL, cathodoluminescence; Defl . X, pair of beam deflection coils in the X direction; Defl . Y, pair of beam deflection coils in the Y direction; Det., detectors; DF-D, dark-field detector; O, specimen; OA, objective aperture; OL, objective lens; PC, personal computer; SE, secondary electrons; STEM, scanning transmission electron microscope signal; W, Wehnelt cylinder; X-ray, X-ray signal. [52]

The signals may vary from one location to another as the electron– specimen interaction changes due to, e.g., topography and specimen composition. The magnification of the image is given by the ratio of the length of the scan on the monitor and the corresponding length of the scan on the specimen. For example, an increase in magnification can simply be achieved by decreasing the current of the deflection coils in the microscope column (i.e., lowering the length of the scan on the specimen) and keeping the image size on the monitor constant. It should be mentioned that the magnification also depends on the WD, however, modern SEMs compensate automatically for each WD, thus keeping the displayed magnification correct. Figure 2.12 shows a series of images recorded with increasing magnifications over a range of almost three orders of magnitude.

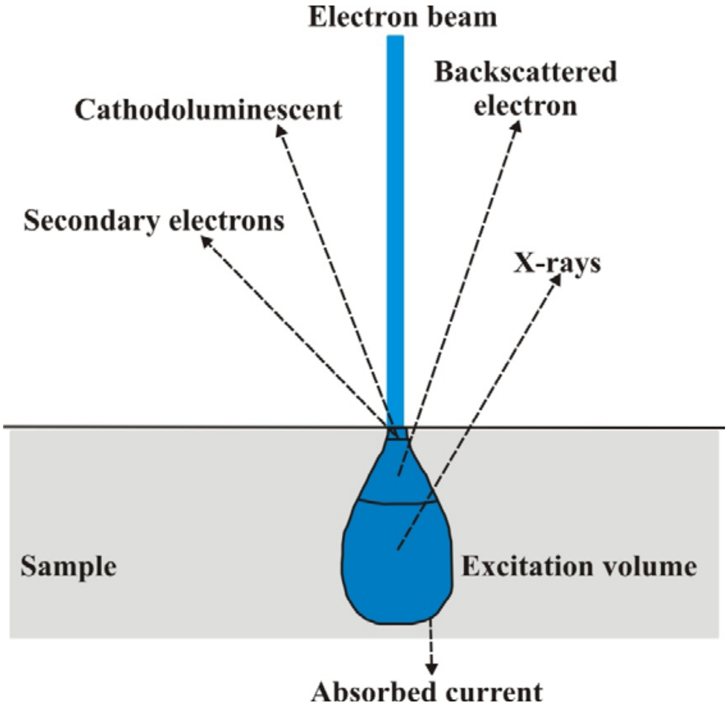

Figure 2.12 Schematic drawing of signals for a thin sample generated by the impinging electrons. [53]

One of the greatest strengths of the SEM is the tremendous depth of focus, i.e., the range of heights of the specimen being simultaneously in focus (figure 2.13). Due to the small objective aperture diaphragm (about 50–100 μm) and the large WD the semiangle of the convergent impinging electron probe is in the order of 10 mrad only. At magnifications that are comparable to those of light microscopy (e.g., 1000×) the SEM has a depth of focus that is about 100 times greater than that of an optical microscope, obviously because the semiangle of convergence is much larger in the latter case.

To take full advantage of all the information that SEM can provide, an understanding of its operation modes and the influence of electron beam parameters on the image resolution, the image contrast, the signal strength, and the S/N ratio as well as the electron–specimen interaction is mandatory. The remarkable success of scanning electron microscopy over several decades is mainly due to the tremendous depth of focus, the brilliant image contrast, and the relatively straightforward sample preparation for imaging of surfaces, and, in combination with X-ray microanalytical equipment, its capability of local quantitative element analysis of specimens.

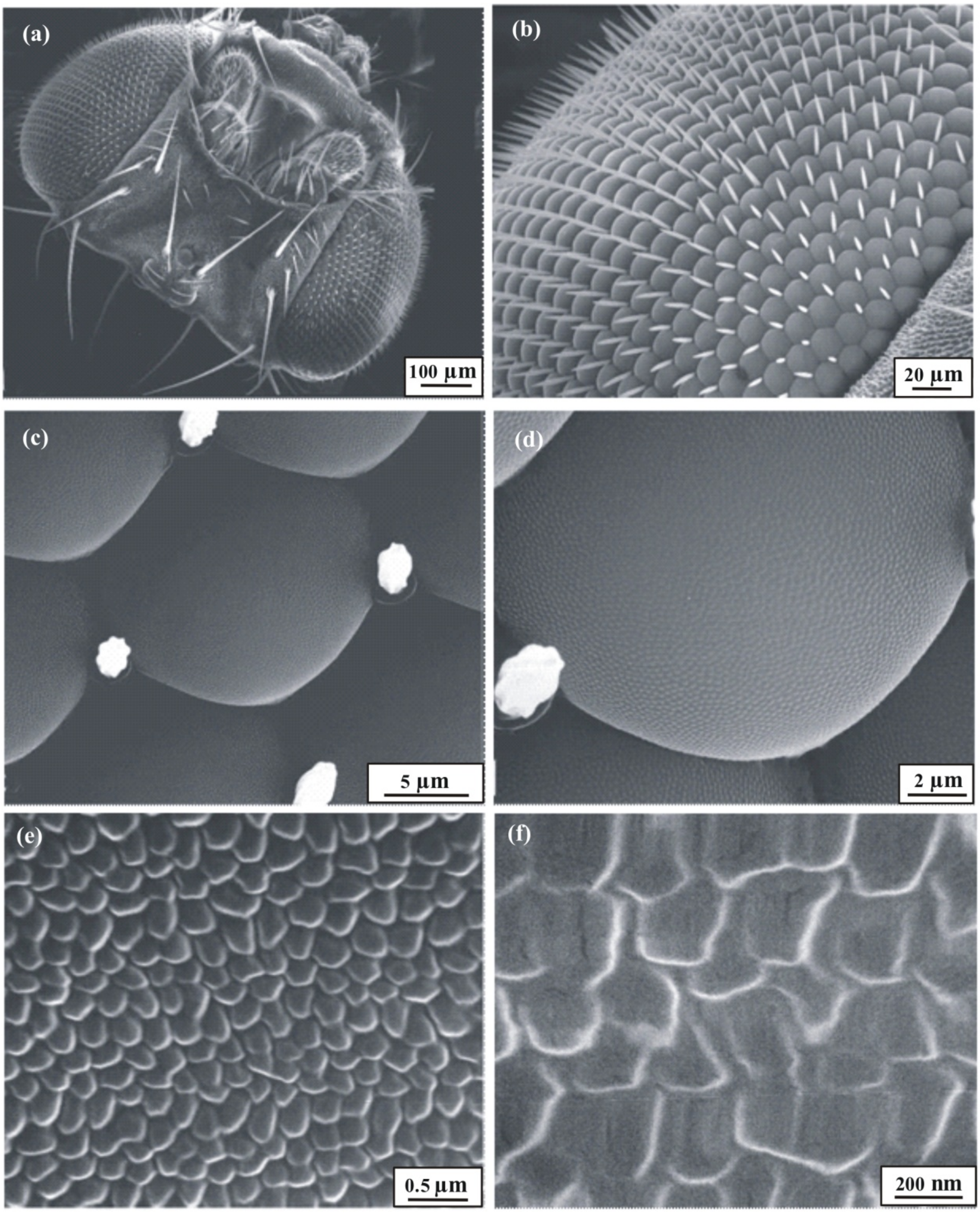

Figure 2.13 Micrograph series of increasing magnification of the head and the eye of a fly, recorded with secondary electrons at 30 kV. The specimen was air dried and sputter coated with about 15 nm gold. Note the large depth of focus. The last magnification step from (e) to (f) barely reveals further fine details of the specimen because of the preparation used. The scale of dimensions of the micrographs covers about three orders of magnitude. [52]

2.10.2 Energy Dispersive Spectroscopy [52]

The structure of EDS in an electron microscope is illustrated as in Figure 2.14, using an SEM system as an example. EDS in the SEM is fundamentally similar to a stand-alone EDS except for the primary beam source. In the SEM, the electron beam aligns with the vertical axis of the microscope so that the Si(Li) detector has to be placed at a certain angle from vertical. The angle between the surface plane of the specimen and detector is called the take-off angle and is often referred to as the angular position of the detector. The take-off angle can be changed by rotating the specimen surface with respect to the detector. For a low take-off angle, a rough surface may interfere with collection of X-ray photons emitted from a valley area as illustrated in Figure 2.14. Such problems do not occur if the specimen has a microscopically flat surface. Although the ability to focus the electrons as a probe enables us to analyze chemical elements in a microscopic area, we should know that the minimum specimen area that EDS can resolve is not equal to the diameter of the electron probe.

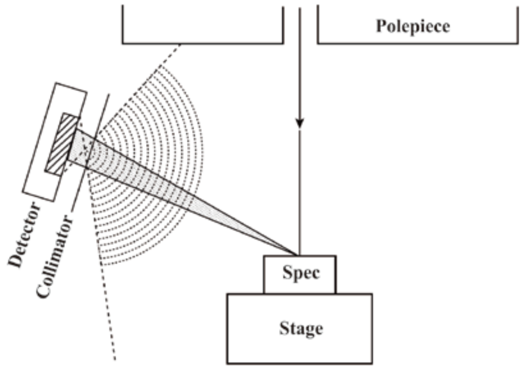

Figure 2.14 Geometrical arrangement of EDS in a scanning electron microscope (SEM) [52].

The characteristic X-rays are excited from a volume under the surface of the specimen, not from an area on the surface. As shown in Figure 2.15, the volume is pear-shaped and its lateral size can be significantly larger than the size of the probe. It is important for us to know, when analyzing a microscopic area of a bulk specimen in an SEM, that EDS signals are emitted from a lateral area that is much larger than the probe diameter. Thus, the spatial resolution of EDS should be considered when we are interested in elemental analysis of a microscopic feature in the SEM.

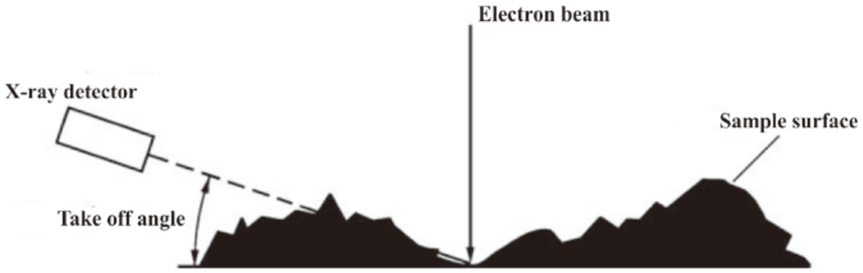

Figure 2.15 Potential interference of X-ray detection due to low take-off angle in the SEM [52].

2.10.3 X-ray diffraction method (XRD) [54]

X-ray diffraction methods are the effective methods for determining the crystal structure of materials. Diffraction methods can identify chemical compounds from their crystalline structure, not from their compositions of chemical elements. It means that the different compounds (or phases) that have the same composition can be identified. Diffraction methods include x-ray diffraction, electron diffraction and neutron. X-ray diffraction by crystals was discovered in 1912, and since then it has been the most extensively studied and used technique for materials characterization.

X-rays are electromagnetic waves, as are visible light, but the x-ray wavelength is much shorter than visible light, only in the order of 0.1 nm. X-ray diffraction methods are based on the phenomenon of wave interferences. Two light waves with the same wavelength and traveling in the same direction can either reinforce or cancel each other, depending on their phase difference. When they have a phase difference of $n\lambda$ (n is an integer), called ‘in phase’, constructive interference occurs. When they have a phase difference of $n\lambda/2$, called ‘completely out of phase’, completely destructive interference occurs.

X-ray beams incident on a crystalline solid will be diffracted by the crystallographic planes as illustrated in figure 2.16. Two in-phase incident waves, beam 1 and beam 2, are deflected by two crystal planes (A and B). The deflected waves will not be in phase except when the following relationship is satisfied.

$$n\lambda = 2d \sin\theta \tag{2.23}$$

where n is an integer, λ is the wavelength of incident wave, d is the spacing between the planes in the atomic lattice, and θ is the angle between the incident ray and the scattering planes(incident angle).

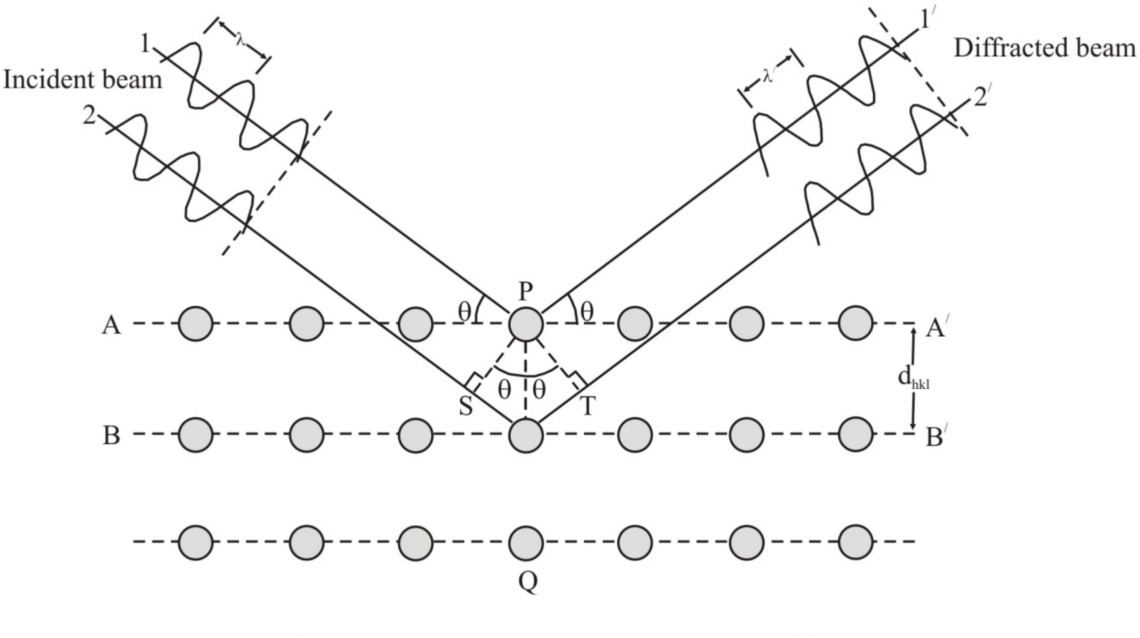

Figure 2.16 Bragg diffraction by crystal planes. The path difference between beams 1 and 2 is $SQ + QT = 2\,PQ \sin\theta$ [54]

Equation 2.22 is the basic law of diffraction called Bragg's Law. Bragg's Law can be simply obtained by calculating the path differences between the two beams in figure 2.16. The path difference depends on the incident angle (θ) and spacing between the parallel crystal planes (d). In order to keep these beams in phase, their path difference ($SQ + QT = 2d \sin\theta$) has to equal one or multiple X-ray wavelengths ($n\lambda$).

We are able to obtain information on the spacing between atomic planes of a crystal when constructive interference is detected at a given incident angle and a wavelength of the incident beam, based on Bragg's Law. Knowing the spacings of crystallographic planes by diffraction methods, we can determine the crystal structure of materials. For example, the plane spacing of cubic crystal relates to the lattice parameter (*a*) by the following equation 2.23.

$$d_{hkl} \qquad = \qquad \frac{a}{\sqrt{h^2 + k^2 + l^2}} \tag{2.24}$$

The Miller indices (hkl) represent a series of parallel planes in a crystal with spacing of d_{hkl} . Combining Equations 2.22 and 2.23, we obtain the following relationship between diffraction data and crystal parameters for a cubic crystal system.

$$\sin^2\theta \qquad = \qquad \frac{\lambda^2}{4a^2}\left(h^2 + k^2 + l^2\right) \tag{2.25}$$

Equation 2.23 does not directly provide the Miller indices of crystallographic planes. We need to convert ($h^2 + k^2 + l^2$) to (hkl) or {hkl}. This should not be difficult for low-index planes of cubic systems. For example, when ($h^2 + k^2 + l^2$) is equal to 1, the plane index must be {001}; when it is equal to 2, the index must be {110}. This type of calculation is often not necessary because the relationship between deflection angle and the Miller indices of most crystalline materials, for a given λ, have been determined and published by the International Centre for Diffraction Data.

2.10.4 Ultraviolet spectroscopy [52]

1) The nature of electronic excitation

Most organic molecules and functional groups are transparent in the portions of the electromagnetic spectrum which we call the ultraviolet (UV) and visible (VIS) regions- that is, the regions where wavelength form 190 nm to 800 nm. Consequently, absorption spectroscopy is of limited utility in this range of wavelengths. However, in some cases we can derive useful information from these regions of the spectrum.

When continuous radiation passes through transparent materials, a portion of the radiation may be absorbed. If that occurs, the residual radiation, when it is passed through a prism, yields a spectrum with gaps in it, called an absorption spectrum. As a result of energy absorption, atoms or molecules pass from a state of low energy (the initial, or ground state) to a state of higher energy (the excited state). Figure 2.17 depicts this excitation process, which is quantized. The electromagnetic radiation that is absorbed has energy exactly equal to the energy difference between the excited and ground state.

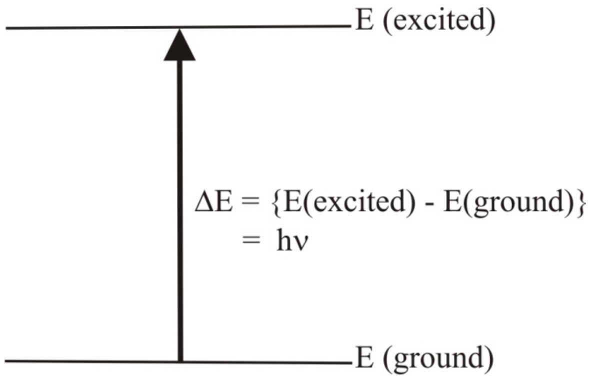

Figure 2.17 The excitation process; E = energy of photon (J), h = Planck's constant (6.626×10^{-34} J/s) and ν = frequency (Hz) of its associated electromagnetic wave. [52]

In the case of ultraviolet and visible spectroscopy, the transition that results in the absorption of electromagnetic radiation in this region of the spectrum are transitions between electronic energy levels. As a molecule absorbs energy, an electron is promoted from an occupied orbital to an unoccupied orbital of greater potential energy. Generally, the most probable transition is from the highest occupied molecular (HOMO) to the lowest unoccupied molecular orbital (LUMO). The energy differences between electronic levels in most molecules vary from 125 to 650 kJ/mole.

For most molecules, the lowest-energy occupied molecular orbitals are the σ bonds. The π orbitals lie at somewhat higher energy levels, and orbitals that hold unshared pairs, the nonbonding (π) orbitals, lie at even higher energies. The unoccupied, or antibonding orbitals (π* and σ*), are the orbitals of highest energy. Figure 2.18(a) shows a typical progression of electronics energy levels.

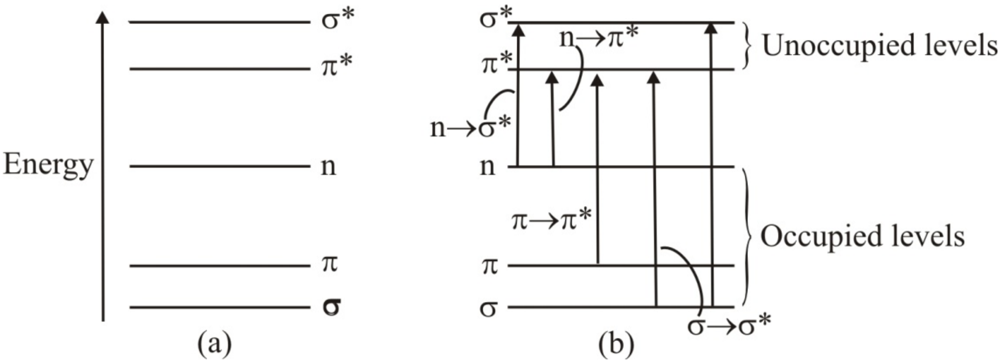

Figure 2.18 Electronic energy levels and transitions [52]

Clearly, the energy required to bring about transitions from the highest occupied energy level (HOMO) in the ground state to the lowest unoccupied energy level (LUMO) is less than the energy required to bring about a transition from lower occupied energy level. Thus, in figure 2.18(b) an $n \rightarrow \pi^*$ transition would have a lower energy than a $\pi \rightarrow \pi^*$ transition. For many purposes, the transition of lowest energy is the most important.

2) The origin of UV band structure

The absorption spectrum sometimes consists of very sharp lines, as would be expected for a quantized process occurring between two discrete energy levels. For molecules, however, the UV absorption usually occurs over a wide range of wavelengths, because molecules (as oppose to atoms) normally have many excited modes of vibration and rotation at room temperature. In fact, the vibration of molecules cannot be completely "frozen out" even at absolute zero. Consequently, a collection of molecules generally has its member in many states of vibrational and rotational excitation. The energy level for these sate are quite closely spaced, corresponding to energy difference considerably smaller than those of electronic level. The rotational and vibrational levels are thus "superimposed" on the electronic levels. A molecule may therefore undergo electronic and vibrational-rotational excitation simultaneously, as show in figure 2.19.

Because there are so many possible transitions, each differing from the others by only a slight amount, each electronic transition consists of a vast number of lines spaced so closely that the spectrophotometer cannot resolve them. Rather, the instrument traces an "envelope" over the entire pattern. What is observed from these types of combined transitions is that the UV spectrum of a molecule usually consists of a broad band of absorption center near the wavelength of the major transition

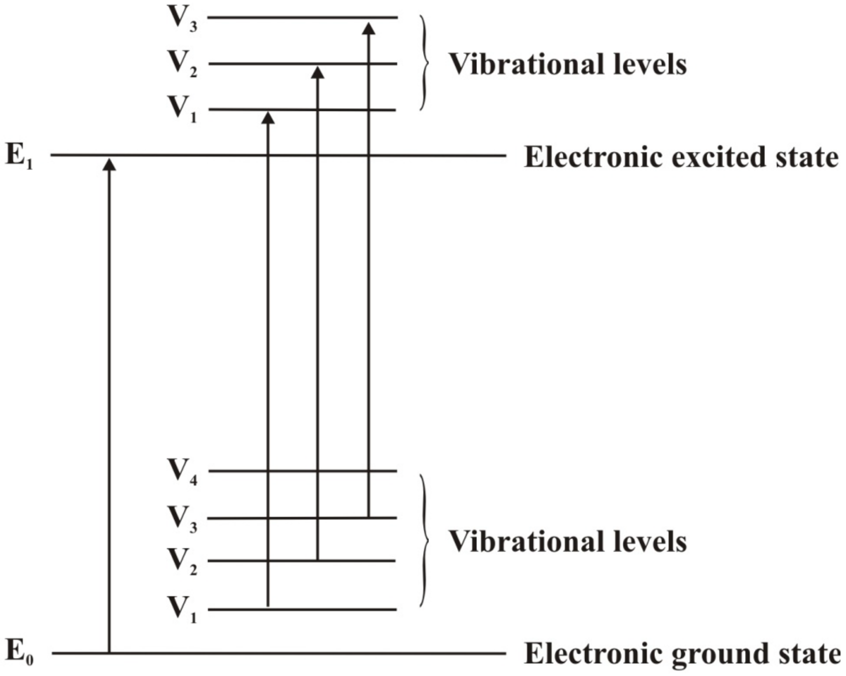

Figure 2.19 Electronic transitions with vibrational transitions superimposed. (Rotational levels, which are very closely spaced within the vibrational levels, are omitted for clarity) [52]

3) Principles of absorption spectroscopy

The greater the number of molecules capable of absorbing light of a given wavelength, the greater the extent of light absorption. Furthermore, the more effectively a molecule absorbs light of a given wavelength, the greater the extent of light absorption. From these guiding ideas, the following empirical expression, known as the Beer-Lambert law, may be formulated.

$$A \quad = \quad \log\left(\frac{I}{I_0}\right) \quad = \quad \varepsilon c \ell \tag{2.26}$$

A = absorbance
I_0 = intensity of light incident upon sample cell
I = intensity of light leaving sample cell
C = molar concentration of solute
ℓ = length of sample cell (cm)
ε = molar absorptivity (L mol^{-1} cm^{-1})

The term $\log\left(\frac{I}{I_0}\right)$ is also known as the absorbance (or the optical density) and may be represented by A. The molar absorptivity (formerly known as the molar extinction coefficient) is a property of the molecule undergoing an electronic transition and is not a function of the variable parameters involved in preparing a solution. The size of the absorbing system and the probability that the electronic transition will take place control the absorptivity, which ranges from 0 to 10^6. Values above 10^4 are termed high-intensity absorptions, while values below 10^3 are low-intensity absorptions.

2.10.5 X-ray photoelectron spectroscopy (XPS) [55]

1) Electron Spectroscopy

In electron spectroscopy we are concerned with the emission and energy analysis of low-energy electrons (generally in the range 20-2000 eV). These electrons are liberated from the specimen being examined as a result of the photoemission process (in XPS) or the radiationless de-excitation of an ionized atom by the Auger emission process in AES and scanning Auger microscopy (SAM). In the simplest terms, an electron spectrometer consists of the sample under investigation, a source of primary radiation, and an electron energy analyser all contained within a vacuum chamber preferably operating in the ultra-high vacuum (UHV) regime. In practice, there will often be a secondary UHV chamber fitted with various sample preparation facilities and perhaps ancillary analytical facilities. A data system will be used for data acquisition and subsequent processing. The source of the primary radiation for the two methods is different: X-ray photoelectron spectroscopy makes use of soft X-rays, generally AlKα or MgKα, whereas AES and SAM rely on the use of an electron gun. The specification for electron guns used in Auger analysis varies tremendously, particularly as far as the spatial resolution is concerned which, for finely focused guns, may be between 5 um and <10nm. In principle, the same energy analyser may be used for both XPS and AES; consequently, the two techniques are often to be found in the same analytical instrument. Before considering the uses and applications of the two methods, a brief review of the basic physics of the two processes and the strengths and weaknesses of each technique will be given.

2) Notation

XPS and AES measure the energy of electrons emitted from a material. It is necessary, therefore, to have some formalism to describe which electrons are involved with each of the observed transitions. The notation used in XPS is different from that used in AES. XPS uses the so-called 'spectroscopists' or 'chemists' notation while Auger electrons are identified by the X-ray notation.

3) Spectroscopists' notation

In this notation the photoelectrons observed are described by means of their quantum numbers. Transitions are usually labelled according to the scheme nl_j. The first part of this notation is the principal quantum number, n. This takes integer values of 1, 2, 3 etc. The second part of the nomenclature, l is the quantum number which describes the orbital angular momentum of the electron. This takes integer values 0, 1, 2, 3 etc. However, this quantum number is usually given a letter rather than a number as shown in Table 25.

Table 2.5 Notation given to the quantum numbers which describe orbital angular momentum[55]

Value of l	Usual notation
0	s
1	p
2	d
3	f

The peaks in XPS spectra, derived from orbitals whose angular momentum quantum number is greater than 0, are usually split into two. This is a result of the interaction of the electron angular momentum due to its spin with its orbital angular momentum. Each electron has a quantum number associated with its spin angular momentum, s^2. The value of s can be either +1/2 or -1/2. The two angular momenta are added vectorially to produce the quantity *j* in the expression nl_j i.e., $j = |1 + s|$. Thus, an electron from a p orbital can have a j value of 1/2 (l - s) or 3/2 (l + s); similarly, electrons from a d orbital can have j values of either 3/2 or 5/2. The relative intensity of the components of the doublets formed by the spin orbit coupling is dependent upon their relative populations (degeneracies) which are given by the expression (2j + 1) so, for an electron from a d orbital, the relative intensities of the 3/2 and 5/2 peaks are 2:3. The spacing between the components of the doublets depends upon the strength of the spin orbit coupling. For a given value of both n and l the separation increases with the atomic number of the atom. For a given atom, it decreases both with increasing n and with increasing l. Figure 2.20 shows an XPS spectrum from Sn with the peaks labeled according to this notation and illustrating the splitting observed in the peaks due to electrons in 3p and 3d orbitals while splitting in the 4d and 4p peaks is too small to be observed.

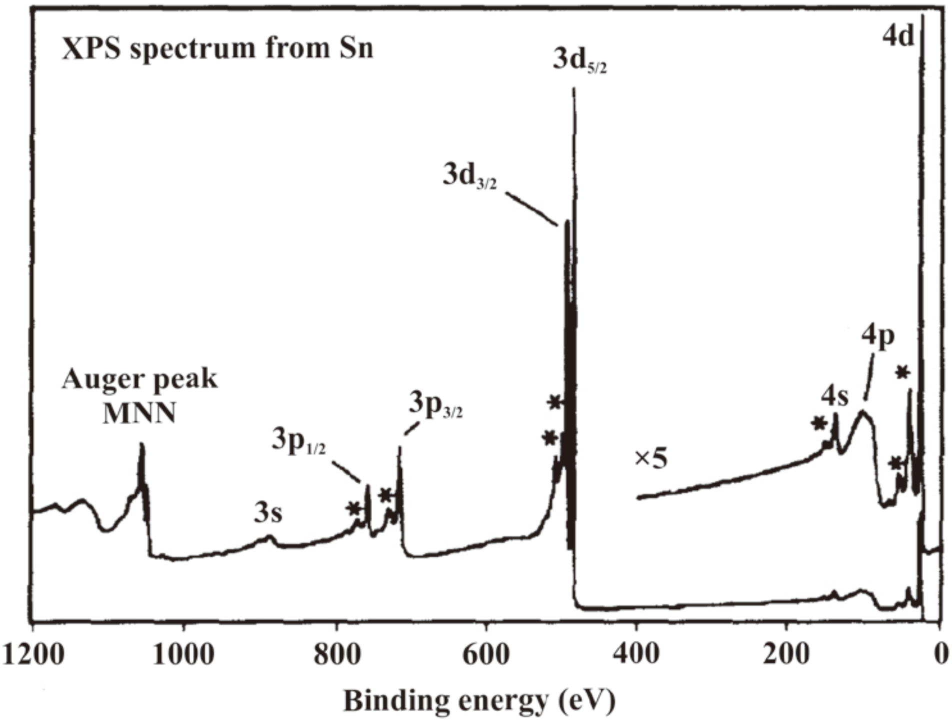

Figure 2.20 Survey spectrum from Sn showing the XPS transitions accessible using AlKα radiation, the features marked with an asterisk are electron energy loss features due to plasmon excitation [55]

4) X-ray notation

In X-ray notation, the principal quantum numbers are given letters K, *L*, M, etc. while subscript numbers refer to the j values described above. The relationship between the notations is given in Table 2.6.

Table 2.6 The relationship between quantum numbers, spectroscopists' notation and X ray notation [55]

Quantum number				Spectroscopists notation	X-ray notation
n	l	s	j		
1	0	+1/2, -1/2	1/2	$1s_{1/2}$	K
2	0	+1/2, -1/2	1/2	$2s_{1/2}$	L_1
2	1	+1/2	1/2	$2p_{1/2}$	L_2
2	1	-1/2	3/2	$2p_{3/2}$	L_3
3	0	+1/2, -1/2	1/2	$3s_{1/2}$	M_1
3	1	+1/2, -1/2	1/2	$3p_{1/2}$	M_2
3	1	-1/2	3/2	$3p_{3/2}$	M_3
3	2	+1/2	3/2	$3d_{3/2}$	M_4
3	2	-1/2	5/2	$3d_{5/2}$	M_5
					etc

As will be seen later, the Auger process involves three electrons and so the notation has to take account of this. This is done simply by listing the three electrons; a peak in an Auger spectrum may be labelled, for example, KL_1L_3 or $L_2M_5M_5$. For convenience, the subscripts are sometimes omitted.

In XPS we are concerned with a special form of photoemission, i.e., the ejection of an electron from a core level by an X-ray photon of energy hv. The energy of the emitted photoelectrons is then analysed by the electron spectrometer and the data presented as a graph of intensity (usually expressed as counts or counts/s) versus electron energy - the Xray induced photoelectron spectrum. The kinetic energy (E_K) of the electron is the experimental quantity measured by the spectrometer, but this is dependent on the photon energy of the X-rays employed and is therefore not an intrinsic material property. The binding energy of the electron (E_B) is the parameter which identifies the electron specifically, both in terms of its parent element and atomic energy level. The relationship between the parameters involved in the XPS experiment is

$$E_B = h\nu - E_K - W \tag{2.27}$$

where hν is the photon energy, E_K is the kinetic energy of the electron, and W is the spectrometer work function. As all three quantities on the right-hand side of the equation are known or measurable, it is a simple matter to calculate the binding energy of the electron. In practice, this task will be performed by the control electronics or data system associated with the spectrometer and the operator merely selects a binding or kinetic energy scale whichever is considered the more appropriate. The process of photoemission is shown schematically in figure 2.21, where an electron from the K shell is ejected from the atom (a Is photoelectron). The photoelectron spectrum will reproduce the electronic structure of an element quite accurately since all electrons with a binding energy less than the photon energy will feature in the spectrum. This is illustrated in figure 2.22 where the XPS spectrum of lead is superimposed on a representation of the electron orbitals.

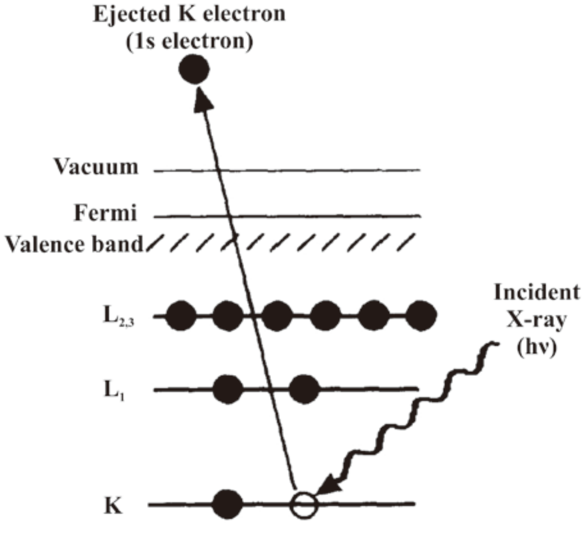

Figure 2.21 Schematic diagram of the XPS process, showing photoionization of an atom by the ejection of a 1s electron[55]

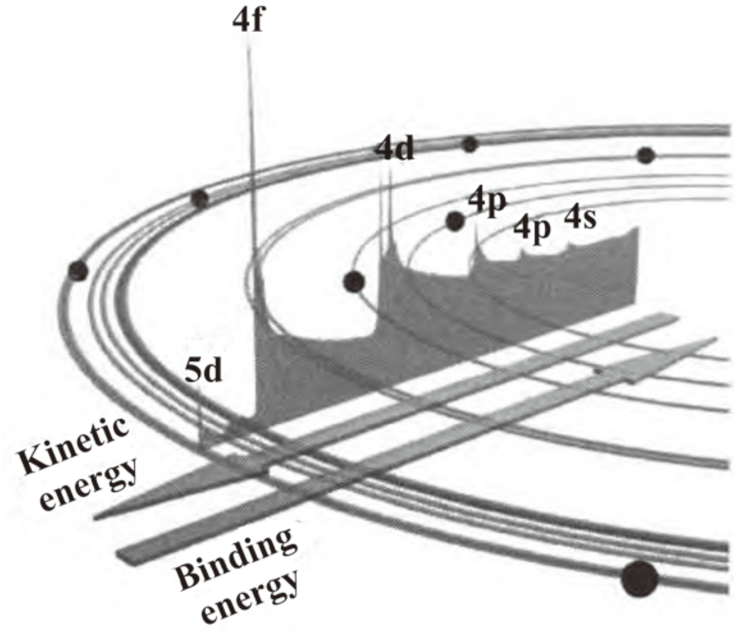

Figure 2.22 Photo electron spectrum of lead showing the manner in which electrons escaping from the solid can contribute to discrete peaks or suffer energy loss and contribute[55]

Those electrons which are excited and escape without energy loss contribute to the characteristic peaks in the spectrum; those which undergo inelastic scattering and suffer energy loss contribute to the background of the spectrum. Once a photoelectron has been emitted, the ionized atom must relax in some way. This can be achieved by the emission of an X-ray photon, known as X-ray fluorescence. The other possibility is the ejection of an Auger electron. Thus Auger electrons are produced as a consequence of the XPS process often referred to as X-AES (X-ray induced Auger electron spectroscopy). X-AES, although not widely practised, can yield valuable chemical information about an atom. For the time being we will restrict our thoughts to AES in its more common form, which is when a finely focused electron beam causes the emission of Auger electrons.